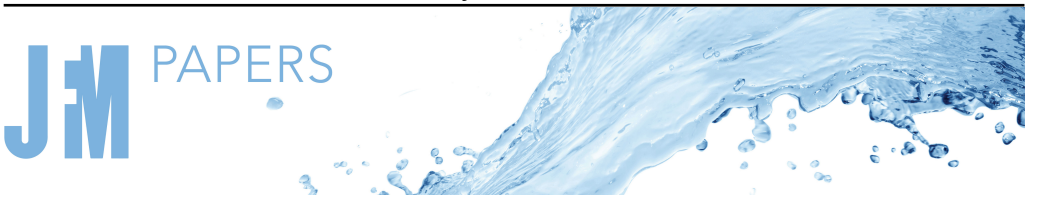
J. Fluid Mech. (2025), *vol.* 1016, A21, doi:10.1017/jfm.2025.10393



Transition regimes of gravity current: from salinity-driven to particle-driven

Jiafeng Xie[1] **and Dingyi Pan**[1,2]

[1]State Key Laboratory of Fluid Power and Mechatronic Systems, Department of Engineering Mechanics, Zhejiang University, Hangzhou 310027, PR China

[2]Innovation Center of Yangtze River Delta, Zhejiang University, Jiaxing 314102, PR China

Corresponding author: Dingyi Pan, dpan@zju.edu.cn

(Received 8 October 2024; revised 5 May 2025; accepted 20 June 2025)

The relationship between salinity-driven (SD) and particle-driven (PD) gravity currents has long been a focal point of geophysical research. This study investigates salinity–particle dual-driven gravity currents using a direct numerical simulation discrete element method. The transition regime from SD to PD currents is explored. The results show that the transition is related to interfacial instability and material transport dynamics. During this transition, the enhancement of particle sedimentation weakens the interfacial stratification and heightens its susceptibility to shear instability. Consequently, the instability generates a series of billows that encourages fluid dilution, further amplifying the particle sedimentation effect. The transition regime is closely associated with this positive closed-loop feedback mechanism. It supplies sufficient energy at the slumping stage to maintain the front velocity of particle-dominated currents comparable to that of salinity-dominated currents. The interfacial vortices will expand spatially by the centrifugal forces on the particles, leading to a reduction in detrainment.

Key words: gravity currents, particle/fluid flow

1. Introduction

Gravity current is a flow event driven by horizontal pressure gradient. This pressure gradient can originate from horizontal density differences caused by variations in temperature, salinity, etc. or from the settlement of suspended particles (Meiburg, Radhakrishnan & Nasr-Azadani 2015). The corresponding flows are known as compositional gravity current, of which salinity-driven (SD) gravity current is taken as an example in this work, as well as particle-driven (PD) gravity current. Such flow occurs widely in natural environments, such as turbidity currents on deep-sea continental slopes, saltwater mazes at estuaries, sandstorms in the atmosphere, etc. A thorough

© The Author(s), 2025. Published by Cambridge University Press.

https://doi.org/10.1017/jfm.2025.10393 Published online by Cambridge University Press

investigation of gravity current is of great significance for understanding material transport and deposition processes in the environment, as well as exposing dynamic processes in ocean and estuarine areas (Parker, Fukushima & Pantin 1986; Böttner *et al.* 2024).

Numerous researchers (Bonnecaze, Huppert & Lister 1993; Necker *et al.* 2005; He *et al.* 2018) have long been interested in the similarities and differences in the dynamic processes between PD and SD gravity current. The main dynamic processes of both are controlled by gravity, and both include core features such as stratification, mixing and convection. However, PD gravity current is distinct from SD gravity current due to the complex settling behaviour of the particles and the intricate fluid–particle interactions.

The front velocity of the gravity current in the early stages is approximately independent of the particle settling velocity (Nasr-Azadani & Meiburg 2014; He *et al.* 2018). The longitudinal length of the current increases linearly in proportion to time t when invading shallow ambient fluids (Bonnecaze *et al.* 1993), corresponding to the constant-velocity slumping stage. After that, the increase in particle settling velocity leads to the acceleration of particle deposition, which reduces the driving force and ultimately the forward velocity of the current (Bonnecaze *et al.* 1993; Huang, Imran & Pirmez 2008; Nasr-Azadani & Meiburg 2014; Nasr-Azadani, Meiburg & Kneller 2018) – it will reduce the flow height near the head (Nasr-Azadani & Meiburg 2014) and weaken the backflow formed by the lock-exchange current (Huang *et al.* 2008). As the particle settling velocity increases from zero, the density stratification close to the interface weakens, increasing the generation of turbulent kinetic energy and resulting in a decreasing velocity gradient (Kneller *et al.* 2016). Thus, the gradient Richardson number decreases, making the current interface more unstable (Kneller *et al.* 2016; Nasr-Azadani *et al.* 2018). According to He *et al.* (2018), the particle settling velocity has no bearing on the current entrainment. They attributed it to the balance between the entrainment enhancement induced by the weakening of stratification and the entrainment weakening caused by the decrease in current velocity, which is consistent with the conclusion of Nasr-Azadani *et al.* (2018). Generally, the evolution characteristics of PD current and SD current during the acceleration phase do not differ significantly. The distinction between these two becomes more noticeable after they reach the slumping stage with a constant forward velocity, which is typically ascribed to the particle sedimentation effect. However, the specific mechanism of particle settling on current is not yet clear.

In addition, this begs the question: How are PD gravity current and SD gravity current associated with one another? Clarifying this transition regime is essential to comprehending the dynamics of gravity current. In real environments like estuaries and marine sedimentary areas, particles and salinity often influence the evolution of gravity current simultaneously, creating a complex phenomenon known as salinity–particle dual-driven (SPDD) gravity current. The two factors may coexist and interact to produce more intricate flow phenomena. Some researchers have become intrigued by this phenomenon since the late 20th century (Gladstone & Woods 2000; Huang *et al.* 2008) and theoretically and experimentally investigated its mechanism. Previous research has shown that the PD current has a stronger turbulent wake region on the current interface and reaches higher elevation than the SPDD current, despite moving more slowly. They ascribed the discrepancy to the varying densities of interstitial fluid. Currently, more research is required to fully comprehend how the interstitial fluid influences the current evolution.

In the manner of mathematical modelling of gravity current, it is possible to degenerate the convection–diffusion equation of PD current to the case of SD current by assuming that the particle phase is regarded as a continuous medium and the particle settling velocity is considered to be zero (Kneller *et al.* 2016). Alternatively, the discrete element method (DEM) has emerged as a new tool for studying particle motion in PD current

https://doi.org/10.1017/jfm.2025.10393 Published online by Cambridge University Press

(Jing *et al.* 2019; Xie *et al.* 2023*a*,*b*; Lu *et al.* 2024) in recent years. Accurately describing the forces acting on each particle and tracking particles' trajectory are two benefits of this method that can aid in a thorough analysis of the fluid–particle interaction during the current, especially that between varying interstitial fluids and particles. Based on this, this work develops a direct numerical simulation (DNS)-DEM coupled model to analyse the coupling between miscible fluid systems and discrete particles, specifically focusing on SPDD gravity currents. Previous studies have developed numerical models for SP coupled gravity currents (Shringarpure, Cantero & Balachandar 2015; He *et al.* 2019). Unlike the Eulerian–Eulerian model used in prior research, our simulation of the fluid phase does not rely on the Boussinesq assumption. We employ the concentration transport equation to describe salinity convection–diffusion behaviour, consistent with the approach adopted by He *et al.* (2019), rather than treating salinity as constant as Shringarpure *et al.* (2015) did. Furthermore, we utilize DEM to simulate the behaviour of discrete particles, whereas earlier studies typically employed the concentration transport equation to describe sediment transport under the assumption of negligible sediment response time. In § 2, the numerical model is introduced. The transition regimes between PD and SD gravity currents are revealed in § 3. Lastly, § 4 provides the conclusions.

2. Description of numerical method

2.1. *Governing equations*

A DNS-DEM coupled model is developed to simulate the SPDD gravity current. Direct numerical simulation is responsible for modelling the miscible fluid, and DEM is for the particle motion. The Navier–Stokes equations without the Boussinesq approximation are employed in DNS as follows:

$$\frac{\partial \alpha_f \rho_f}{\partial t} + \boldsymbol{\nabla} \boldsymbol{\cdot} (\alpha_f \rho_f \boldsymbol{u}_f) = 0, \tag{2.1}$$

$$\frac{\partial \alpha_f \rho_f \boldsymbol{u}_f}{\partial t} + \boldsymbol{\nabla} \boldsymbol{\cdot} (\alpha_f \rho_f \boldsymbol{u}_f \boldsymbol{u}_f) = -\alpha_f \boldsymbol{\nabla} p + \alpha_f \rho_f \boldsymbol{g} + \alpha_f \, \boldsymbol{\nabla} \boldsymbol{\cdot} \boldsymbol{\tau} - \boldsymbol{R}_{pf}, \tag{2.2}$$

where α_f is the volume fraction of the fluid phase, in which $\alpha_f = 1 - \alpha_p$ with α_p being the particle volume fraction; $\rho_f = \alpha_s \rho_s + \alpha_w \rho_w$ is the fluid density with α_s and α_w denoting the relative volume fractions of saline fluid and water, respectively, which represent the proportion of saline fluid and water in the fluid ($\alpha_s + \alpha_w = 1$) and ρ_s and ρ_w being the densities of saline fluid and water, respectively; $\boldsymbol{u}_f = (u_f, v_f, w_f)$ is the fluid velocity; p is the pressure; $\boldsymbol{g} = (0, 0, -9.81)$ m s^{-2} is the gravitational acceleration; $\boldsymbol{\tau}$ is the fluid stress tensor; $\boldsymbol{R}_{pf}$ is the momentum exchange between fluids and particles.

The salinity transport equation has the following form:

$$\frac{\partial \alpha_f \alpha_s}{\partial t} + \boldsymbol{\nabla} \boldsymbol{\cdot} (\alpha_f \alpha_s \boldsymbol{u}_f) = D_s \, \boldsymbol{\nabla} \boldsymbol{\cdot} \boldsymbol{\nabla} (\alpha_f \alpha_s), \tag{2.3}$$

where D_s is the salt diffusion coefficient.

The translational and rotational motion of individual particles are tracked by the DEM method (Cundall & Strack 1979). Within the DEM framework, the contact force $\boldsymbol{F}^c$ between particles and between particles and wall is solved by the Hertz–Mindlin model which is a linear spring–dashpot model (Cundall & Strack 1979). Parameter values involved in the collision model can be found in our previous paper (Xie *et al.* 2023*b*). The point-force approximation is adopted to determine the fluid–particle interaction forces as $d_p/\eta \ll O(1)$ with d_p the particle diameter and η the Kolmogorov length. Herein, the interaction force $\boldsymbol{F}^f$ encompasses drag force $\boldsymbol{F}^d$, pressure gradient force

https://doi.org/10.1017/jfm.2025.10393 Published online by Cambridge University Press

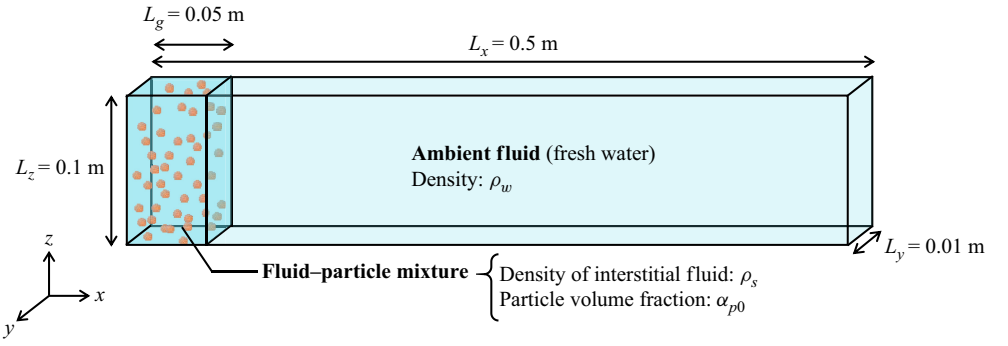


Figure 1. Schematic diagram of the lock-exchange dual-driven gravity current.

$\boldsymbol{F}^{\nabla p}$, viscous force $\boldsymbol{F}^{\nabla\cdot\boldsymbol{\tau}}$, lift force $\boldsymbol{F}^{l}$ and added mass force $\boldsymbol{F}^{add}$. The modelling of the above forces is applicable in this study to cases where the particle Reynolds number $Re_p = |\boldsymbol{u}_f - \boldsymbol{u}_p| d_p/\nu_f$ is of the order of $O(10^{-1})$, where $\boldsymbol{u}_p$ is the particle velocity and ν_f is the kinematic viscosity. With the exception of the pressure gradient force and viscous force, the modelling formulae for the other forces agree with our earlier research (Xie *et al.* 2023*a*,*b*). The pressure gradient force and viscous force are formulated by (Zhou *et al.* 2010)

$$\boldsymbol{F}^{\nabla p} = \frac{1}{6}\pi d_p^3 \nabla p, \quad \boldsymbol{F}^{\nabla\cdot\boldsymbol{\tau}} = \frac{1}{6}\pi d_p^3 \nabla\cdot\boldsymbol{\tau}. \tag{2.4}$$

The total force acting on a particle can be expressed by $\boldsymbol{F}^T = \boldsymbol{F}^d + \boldsymbol{F}^{\nabla p} + \boldsymbol{F}^{\nabla\cdot\boldsymbol{\tau}} + \boldsymbol{F}^l + \boldsymbol{F}^{add} + \boldsymbol{F}^c$. During the coupling process, the force exerted by a particle on a given fluid grid depends on the actual volume of the particle within that grid. In addition, as the pressure gradient term and viscous term in (2.2) already include the particle contribution, the momentum exchange $\boldsymbol{R}_{pf}$ only includes drag, lift and added mass forces (see Zhou *et al.* 2010). In the model, fluid properties, such as density and velocity, are interpolated to discrete particle positions using Gaussian interpolation. The point-force model has been validated as an effective method for simulating particle motion in density-stratified fluids (Blanchette 2013). To further illustrate the model's ability to capture particle behaviour in density-varying fluids, we simulate particle settling in a linearly stratified fluid. The results indicate that the model effectively describes the fluid mixing phenomenon induced by particle settling. Additional details are provided in Appendix A.

2.2. *Numerical configurations*

We employ a lock-exchange approach to generate gravity currents, consistent with the methodology used in previous studies (Necker *et al.* 2002; Cantero, Balachandar & Garcia 2008; Espath *et al.* 2015; He *et al.* 2019; Pelmard, Norris & Friedrich 2020). Unlike Shringarpure *et al.* (2012, 2015, 2019), who used streamwise periodic boundaries to study steady-state currents, our simulation captures the acceleration, slumping and deceleration phases of gravity currents. The simulation of the lock-exchange gravity current is conducted in a cuboid domain with dimensions $L_x = 0.5$ m (length), $L_y = 0.01$ m (width) and $L_z = 0.1$ m (height), as shown in figure 1. The streamwise direction of the domain is set as a no-slip boundary, the spanwise direction as a periodic boundary, the top surface as a slip boundary and the bottom surface a no-slip boundary.

https://doi.org/10.1017/jfm.2025.10393 Published online by Cambridge University Press

For the particle phase simulation, the spanwise direction also uses periodic boundaries, aligning with the fluid simulation, and the other surfaces are treated as wall boundaries. The left-hand side of the domain is a lock with a streamwise length of $L_g = 0.05$ m. Initially, the lock is filled with saline or fresh water, with a density of ρ_s and a kinematic viscosity of $\nu_f = 10^{-6}\,\mathrm{m^2\,s^{-1}}$. Additionally, a number of N_p particles, with a density of $\rho_p = 1500\,\mathrm{kg\,m^{-3}}$ and a diameter of $d_p = 100\,\mu\mathrm{m}$, are randomly distributed in the lock, corresponding to an initial particle volume fraction of α_{p0}. Accordingly, the overall initial density of the fluid–particle mixture in the lock is given by $\rho_{m0} = \alpha_{p0}\rho_p + \alpha_{f0}\rho_s$. The region outside the lock is filled with fresh fluid, with a density of $\rho_w = 1000\,\mathrm{kg\,m^{-3}}$ and a kinematic viscosity of $\nu_f = 10^{-6}\ \mathrm{m^2\ s^{-1}}$. The initial density difference between the gravity current and the ambient fluid is expressed as $\Delta\rho = \rho_{m0} - \rho_w = \alpha_{p0}(\rho_p - \rho_w) + \alpha_{f0}(\rho_s - \rho_w) = 3.5\,\mathrm{kg\,m^{-3}}$, where $\alpha_{p0}(\rho_p - \rho_w)$ represents the particle contribution and $\alpha_{f0}(\rho_s - \rho_w)$ is the salinity contribution. Thus, the ratio of the salinity contribution to ρ_{m0} to the particle contribution ξ_{sp} is determined by

$$\xi_{sp} = \frac{\alpha_{f0}(\rho_s - \rho_w)}{\alpha_{p0}(\rho_p - \rho_w)}. \tag{2.5}$$

As the simulation starts, the gate is lifted up and the gravity current is formed and propagates downstream. The local density of fluid–particle mixture is determined by $\rho_m = \alpha_p\rho_p + \alpha_f(\alpha_s\rho_s + \alpha_w\rho_w)$. The front position, x_{front}, is an important parameter describing the gravity current propagation ability. The front of the particle flow is captured by the position of the most downstream particle, and the front of the salinity is identified by the relative volume fraction of saline fluid $\alpha_s = 10^{-4}$.

For dimensionalization, we adopt the buoyancy velocity $u_b = \sqrt{g' L_z/2}$ as the characteristic velocity (Necker *et al.* 2005; Pelmard *et al.* 2020), where the effective gravity acceleration $g' = |\boldsymbol{g}|(\rho_{m0} - \rho_w)/\rho_w$. The characteristic length is taken as half the initial mixture height $L_z/2$, and the characteristic time is given by $L_z/(2u_b)$. The particle mass m_p and the gravity of a particle, $m_p|\boldsymbol{g}|$, are used as the characteristic mass and characteristic force. The density ρ is non-dimensionalized by $\tilde{\rho} = (\rho - \rho_w)/(\rho_{m0} - \rho_w)$. All the dimensionless variables are denoted by a tilde $(\tilde{\cdot})$. Thus, the dimensionless domain sizes are $\tilde{L}_x \times \tilde{L}_y \times \tilde{L}_z = 10 \times 0.2 \times 2$, and the lock length is $\tilde{L}_g = 1$.

This study is carried out with ξ_{sp} as a variable, and the set-ups for cases are shown in table 1. A decrease in ξ_{sp} implies a higher contribution from particles to the gravity current's density difference $\Delta\rho$. There are some dimensionless parameters describing the flow characteristics, including the flow Reynolds number (Re), the Schmidt number (Sc) reflecting the salinity diffusion, the particle Stokes number (St), the Galileo number (Ga), the particle settling Reynolds number ($Re_{p,t}$), the dimensionless particle settling velocity ($\tilde{\gamma}_t$), the dimensionless characteristic settling time ($\tilde{t}_s$), the ratio of time scales ($\tilde{S}$) and the density ratio of particle to fluid ($\tilde{s}_p$), which are given by

$$\begin{gathered} Re = \frac{u_b L_z}{2\nu_f},\quad Sc = \frac{\nu_f}{D_s},\quad St = \frac{\rho_p|\boldsymbol{u}_f - \boldsymbol{u}_p|d_p}{(9\rho_s\nu_f)},\quad Ga = \frac{\sqrt{\rho_p/\rho_f g' d_p^3}}{\nu_f}, \\ Re_{p,t} = \frac{u_t d_p}{\nu_f},\quad \tilde{\gamma}_t = \frac{u_t}{u_b},\quad \tilde{t}_s = \frac{L_z}{u_t}\frac{u_b}{L_z/2},\ \tilde{S} = \frac{L_g}{u_b}\frac{u_t}{L_z},\quad \tilde{s}_p = \frac{\rho_p}{\rho_f}, \end{gathered} \tag{2.6}$$

where D_s is the salt diffusivity, and $u_t = (\rho_p - \rho_s)|\boldsymbol{g}|d_p^2/(18\rho_s\nu_f)$ is the particle settling velocity which is negatively related to ξ_{sp}. In this work, $Re = 2071$, $Sc = 1$, St is of the order of $O(10^{-2})$, Ga is of the order of $O(10^{-1})$, $Re_{p,t}$ is of the order of $O(10^{-1})$, $\tilde{\gamma}_t$

https://doi.org/10.1017/jfm.2025.10393 Published online by Cambridge University Press

	Case 1	Case 2	Case 3	Case 4	Case 5	Case 6	Case 7	Case 8	Case 9
α_{p0} [–]	0	0.001	0.002	0.003	0.0035	0.004	0.005	0.006	0.007
N_p [–]	0	95 493	190 986	286 479	334 225	381 972	477 465	572 958	668 451
$\tilde{\rho}_s$ [–]	1	0.858	0.715	0.572	0.501	0.429	0.286	0.143	0
$\tilde{\gamma}_t$ [$\times 10^{-2}$]	6.508	6.521	6.532	6.543	6.548	6.553	6.562	6.570	6.577
$\tilde{t}_s$ [–]	30.732	30.672	30.617	30.567	30.544	30.521	30.480	30.443	30.410
$\tilde{S}$ [$\times 10^{-2}$]	3.254	3.260	3.266	3.272	3.274	3.276	3.281	3.285	3.288
ξ_{sp} [–]	$+\infty$	6.0	2.5	1.3	1.0	0.75	0.40	0.17	0

Table 1. List of simulations: initial particle volume fraction α_{p0}; particle number N_p; saline fluid density $\tilde{\rho}_s$; dimensionless particle settling velocity $\tilde{\gamma}_t$; dimensionless characteristic settling time $\tilde{t}_s$; ratio of time scales $\tilde{S}$; salinity–particle contribution ratio ξ_{sp}.

is approximately 0.07, $\tilde{t}_s$ is approximately 30, $\tilde{S}$ is approximately 0.03 within the range of Gadal *et al.* (2023) and $\tilde{s}_p$ is approximately 1.5. The reason for selecting the particle density of 1500 kg m^{-3} is to maximize the dimensionless characteristic settling time $\tilde{t}_s$, though $\tilde{t}_s \approx 30$ is approximately one order less than that in the previous studies (Cantero *et al.* 2008; Kneller *et al.* 2016; Nasr-Azadani *et al.* 2018).

The characteristic length used in studies influences buoyancy velocity (u_b) and, consequently, the flow Reynolds number (Re). This study adopts half the initial height ($L_z/2$) as the characteristic length (Necker *et al.* 2002; Tsai & Chou 2025), whereas some previous studies use the full initial height (L_z) (Cantero *et al.* 2007; Marshall *et al.* 2021). In this case, the flow Reynolds number is defined as $Re_L = \sqrt{g' L_z} L_z/\nu_f = 2\sqrt{2}Re$. The flow Reynolds numbers in this study ($Re = 2071$ and $Re_L = 5858$) fall within the ranges reported in previous three-dimensional DNS studies, such as $Re = 316-3164$ in Cantero *et al.* (2007), $Re = 2236-10\,000$ in Necker *et al.* (2002), $Re = 2000-5000$ in Nasr-Azadani & Meiburg (2014), $Re = 35-3536$ in Bonometti & Balachandar (2008) and $Re = 1125-2249$ in a computational fluid dynamics (CFD)-DEM simulation (Tsai & Chou 2025). Provided the dimensionless settling time ($\tilde{t}_s$) remains sufficient, higher Reynolds numbers increase the number of fluid cells and particles in CFD-DEM simulations. Although increasing Reynolds number fragments the turbulent structures (Espath *et al.* 2014, 2015), it does not alter the qualitative understanding. Future research should explore gravity current dynamics in high-Re CFD-DEM simulations in greater depth.

We employ a uniform grid system with a grid resolution of $N_x \times N_y \times N_z = 800 \times 16 \times 160$. The ratio of grid size to particle size $d_{x(yz)}/d_p$ is accordingly 6.25. The ratio of particle size to Kolmogorov length d_p/η is of the order of $O(10^{-4}\sim 10^{-1})$, validating using the point-force approximation (Balachandar 2009), and the ratio of grid size to Kolmogorov length $d_{x(yz)}/\eta$ is of the order of $O(10^{-3}\sim 10^{0})$ with the maximum being the 1.3, demonstrating that the grid resolution is fine enough to capture the turbulence structures (Arthur & Fringer 2014).

For the main two-dimensional characteristics of turbidity currents, spanwise averaging is the main research method. The spanwise-averaged quantities of fluid and particle phases ($\langle \mathcal{Q}^f \rangle$ and $\langle \mathcal{Q}^p \rangle$) are calculated as follows:

$$\langle \mathcal{Q}^f\ (x,\, z) \rangle = \frac{\int \alpha_f\ (x,\, y,\, z)\ \mathcal{Q}^f\ (x,\, y,\, z)\ \mathrm{d}y}{\int \alpha_f\ (x,\, y,\, z)\ \mathrm{d}y}, \tag{2.7}$$

https://doi.org/10.1017/jfm.2025.10393 Published online by Cambridge University Press

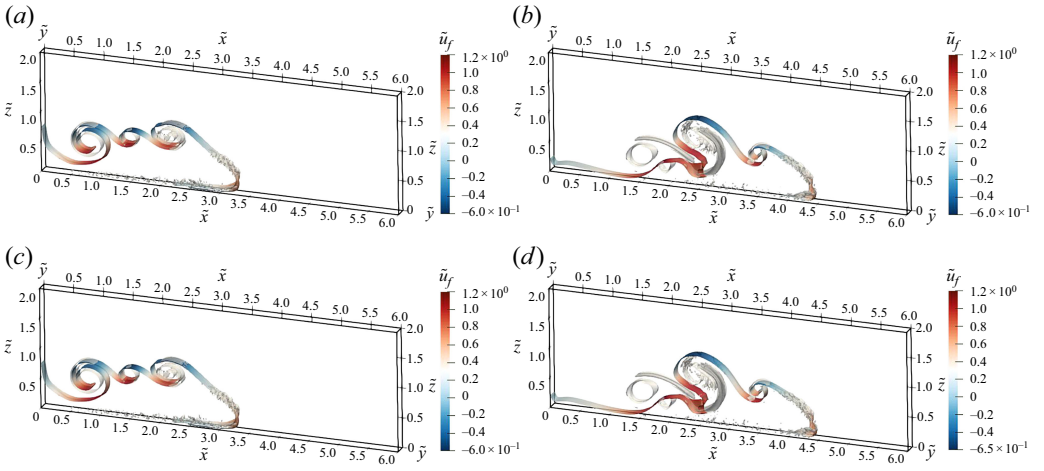


Figure 2. Evolution of $\xi_{sp} = 1.0$ dual-driven current for different Schmidt numbers: (*a*,*b*) $Sc = 1$ and (*c*,*d*) $Sc = 700$; (*a*,*c*) $\tilde{t} = 4$ and (*b*,*d*) $\tilde{t} = 6$. The grey translucent vortex structures are captured using the Q-criterion ($\tilde{Q} = 5$). The saline flow profile is captured with $\alpha_s = 0.5$ and is coloured with the streamwise fluid velocity $\tilde{u}_f$.

$$\langle \mathcal{Q}^p(x,z)\rangle = \frac{1}{N_{p,y}} \sum_{i=1}^{N_{p,y}} \mathcal{Q}_i^p(x,y,z)\,, \qquad x_{p,i} \in \left(x - \frac{L_x}{2N_x}, x + \frac{L_x}{2N_x}\right] \quad \text{and} \quad z_{p,i} \in \left(z - \frac{L_z}{2N_z}, z + \frac{L_z}{2N_z}\right], \tag{2.8}$$

in which $\mathcal{Q}^f$ and $\mathcal{Q}_i^p$ are the fluid variables and the variables of particle i before spanwise averaging, respectively. Here $N_{p,y}$ is the particle number within the selected area.

2.3. *Discussion on the effect of numerical parameters*

The Schmidt number $Sc = 1$ adopted here is lower than $Sc = 700$ corresponding to the salinity diffusion in the oceanic applications (Meiburg *et al.* 2015). Generally, as long as Sc is not less than unity, the current evolution is independent of Sc (Härtel *et al.* 2000; Necker *et al.* 2005; Cantero *et al.* 2007), especially at high Reynolds numbers (Bonometti & Balachandar 2008; Ooi, Constantinescu & Weber 2009). This justifies the use of $Sc = 1$ in many studies for simplicity (Necker *et al.* 2002, 2005; Nasr-Azadani & Meiburg 2014; He *et al.* 2018; Pelmard *et al.* 2020). A recent work by Marshall *et al.* (2021) demonstrated the impact of Sc at low Reynolds numbers of $Re \leqslant 1061$, which is related to structures in the mixed layer between the ambient fluid and the current. The Reynolds number (Re) in this work is 2071, which is higher than the maximum Reynolds number in Marshall *et al.* (2021) but lower than the Reynolds number of 3536, above which Bonometti & Balachandar (2008) pointed out that Sc has no significant effect. Therefore, there may be uncertainty regarding the effect of Sc at the Reynolds number in this study. In view of this, we investigate the effect of Sc on the gravity current evolution. Figure 2 illustrates the three-dimensional profiles and coherent vortex structures of the current under varying Schmidt numbers. Figure 3 shows the spanwise-averaged profiles at different Sc values, including the fluid streamwise velocity $\langle \tilde{u}_f \rangle$, fluid density $\langle \tilde{\rho}_f \rangle$, relative particle volume fraction $\langle \alpha_p \rangle / \alpha_{p0}$, mixture density $\langle \tilde{\rho}_m \rangle$ and gradient Richardson number $\langle Ri_g \rangle$, which is

https://doi.org/10.1017/jfm.2025.10393 Published online by Cambridge University Press

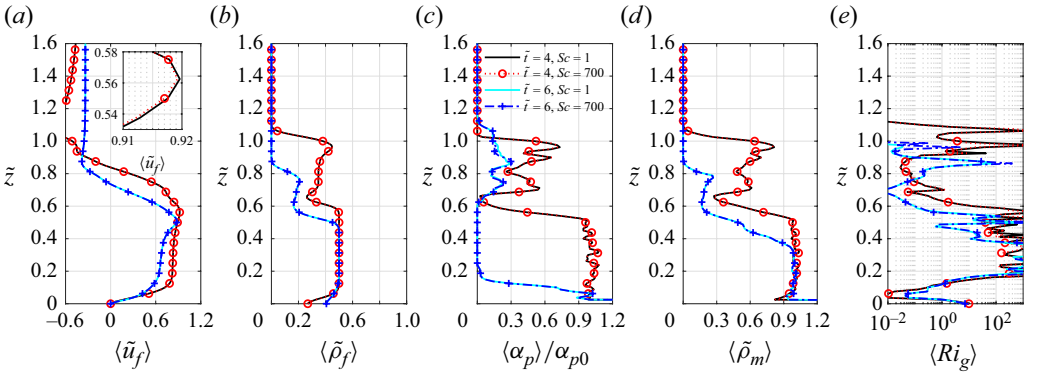


Figure 3. Spanwise-averaged profiles under varying Schmidt numbers ($Sc = 1$ and $Sc = 700$) at different times ($\tilde{t} = 4$ and $\tilde{t} = 6$). Profiles at $\tilde{t} = 4$ are obtained by averaging over $\tilde{x} = 2{\sim}2.4$ and those at $\tilde{t} = 6$ are obtained by averaging over $\tilde{x} = 3.2{\sim}3.6$. (*a*) Fluid streamwise velocity $\langle\tilde{u}_f\rangle$, (*b*) fluid density $\langle\tilde{\rho}_f\rangle$, (*c*) relative particle volume fraction $\langle\alpha_p\rangle/\alpha_{p0}$, (*d*) mixture density $\langle\tilde{\rho}_m\rangle$ and (*e*) gradient Richardson number $\langle Ri_g\rangle$. The inset in panel (*a*) presents a magnified view of the velocity profile to highlight the impact of Sc.

defined as (Kneller *et al.* 2016)

$$\langle Ri_g\rangle = -\frac{|\boldsymbol{g}|\frac{\partial\langle\rho_m\rangle}{\partial z}}{\langle\rho_f\rangle\frac{\partial\langle u_f\rangle}{\partial z}}. \tag{2.9}$$

The figures reveal that, under the Reynolds number considered in the present study, an increase in Sc from 1 to 700 has no significant effect on the flow structures.

Previous studies have shown that two- and three-dimensional configurations yield quantitatively different but qualitatively consistent simulation results (Cantero *et al.* 2007; Ooi *et al.* 2009; Francisco, Espath & Silvestrini 2017; He *et al.* 2018), and some studies typically employed density distributions with random perturbations as initial conditions (Härtel *et al.* 1997; Cantero *et al.* 2007). The influence of computational domain width ($\tilde{L}_y$) and initial disturbance configuration on flow evolution is examined here. Figure 4(*a*,*b*) shows the three-dimensional structures of the SPDD gravity current at $\xi_{sp} = 1.0$ under different computational domain widths ($\tilde{L}_y = 0.2$, 0.8) and initial density distributions, including coherent vortex structures identified by using the Q-criterion and current profiles captured by salinity. Spanwise-averaged profiles for various $\tilde{L}_y$ values ($\tilde{L}_y = 0.2$, 0.4, 0.8) are shown in figure 4(*c*). As the spanwise computational domain expands, the number of grids in the spanwise direction increases proportionally to maintain consistent grid resolution. Comparisons between figures 4(*a*) and 4(*b*) reveal that initial density perturbations have minimal impact on flow structure evolution in this study. The figure also demonstrates that, during the slumping stage, the width of the computational domain exerts negligible influence on the flow dynamics. Three-dimensional simulations across different domain widths consistently exhibit Kelvin–Helmholtz (KH) instabilities at the interface and complex structures at the current head. These flow features are consistent with previous understandings (Cantero *et al.* 2007; Espath *et al.* 2015; Nasr-Azadani *et al.* 2018; Tsai & Chou 2025). As the domain width increases, spanwise variations of these structures, especially the lobes and clefts reflected on the bottom side of the head, become more observable, though qualitative differences remain absent.

https://doi.org/10.1017/jfm.2025.10393 Published online by Cambridge University Press

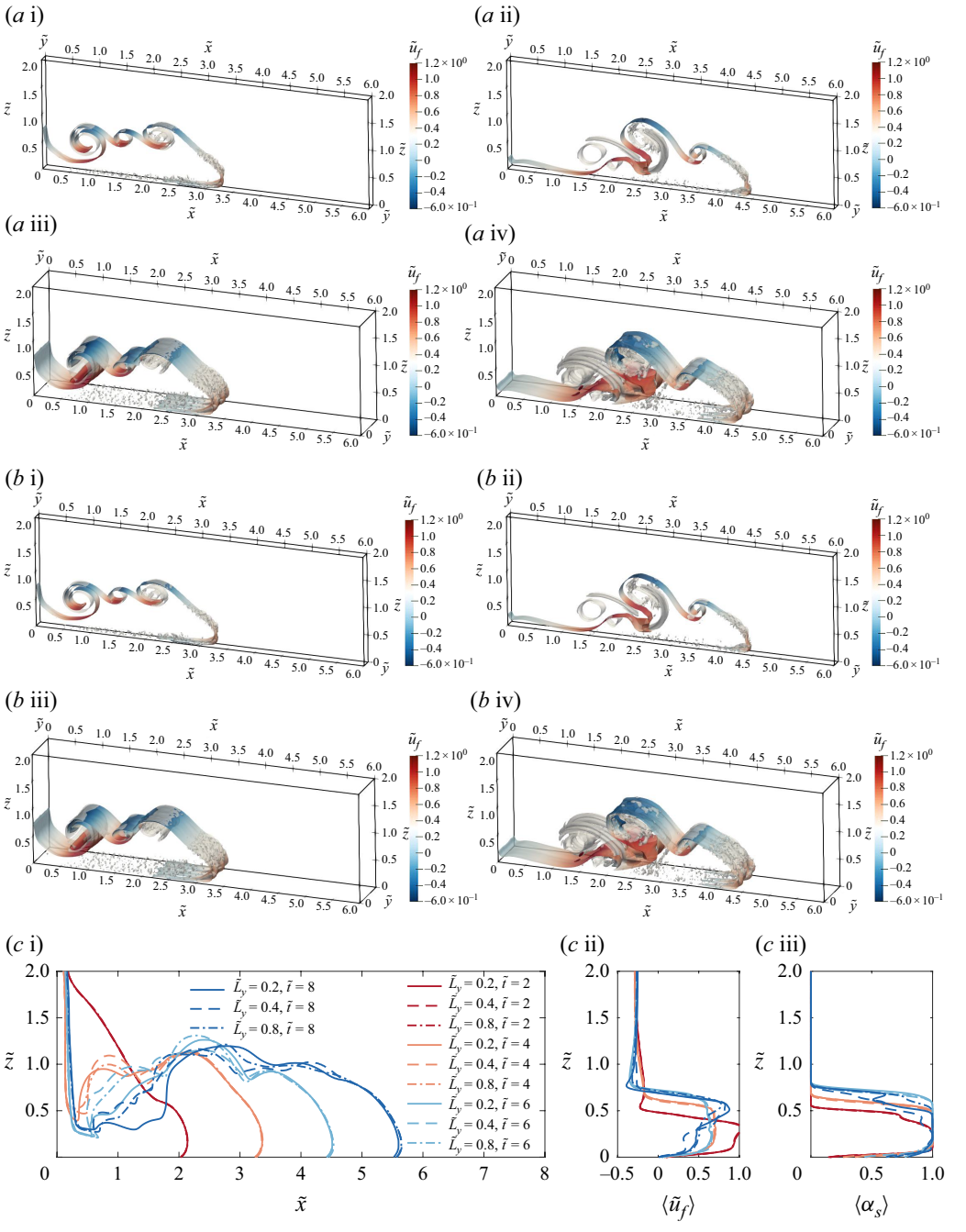


Figure 4. Comparison of current structures at $\xi_{sp} = 1.0$ with different computational domain widths ($\tilde{L}_y$) and initial density distribution conditions. Three-dimensional structures (*a*) without initial disturbance and (*b*) with initial disturbance. Panels (*a* i), (*a* iii), (*b* i) and (*b* iii) correspond to $\tilde{t} = 4$, while panels (*a* ii), (*a* iv), (*b* ii) and (*b* iv) correspond to $\tilde{t} = 6$. Here (*a* i,*a* ii,*b* i,*b* ii) $\tilde{L}_y = 0.2$ and (*a* iii,*a* iv,*b* iii,*b* iv) $\tilde{L}_y = 0.8$. The grey translucent vortex structures are captured using the Q-criterion ($\tilde{Q} = 5$). The saline flow profile is captured with $\alpha_s = 0.5$ and is coloured with the streamwise fluid velocity $\tilde{u}_f$. (*c* i) Spanwise-averaged current profiles identified by $\langle \alpha_s \rangle = 10^{-4}$, (*c* ii) spanwise-averaged fluid streamwise velocity profiles ($\langle \tilde{u}_f \rangle$) and (*c* iii) spanwise-averaged salinity profiles ($\langle \alpha_s \rangle$) for various $\tilde{L}_y$ values at $\tilde{x} = 0.85\tilde{x}_{front}$ and at $\tilde{t}$ =2, 4, 6 and 8.

https://doi.org/10.1017/jfm.2025.10393 Published online by Cambridge University Press

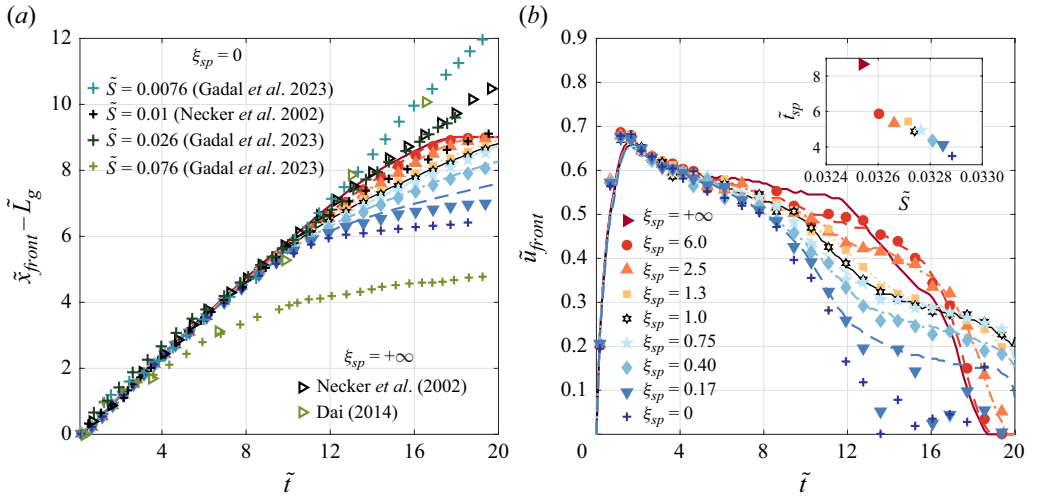


Figure 5. Temporal evolution of (*a*) front position $\tilde{x}_{front}-\tilde{L}_g$ and (*b*) front velocity $\tilde{u}_{front}$. The lines indicate the front position and velocity given by the salinity contour, and the data marked in symbols is obtained from the most downstream particle's position. The inset in panel (*b*) shows the duration of slumping stage $\tilde{t}_{sp}$ at different $\tilde{S}$s.

3. Results

3.1. *Current front and morphological patterns*

Figure 5 presents the time evolution of the current front position $\tilde{x}_{front}-\tilde{L}_g$ and front velocity $\tilde{u}_{front}$, calculated as $\tilde{u}_{front}=\mathrm{d}\tilde{x}_{front}/\mathrm{d}\tilde{t}$, of the particle and salinity flow. In order to access the duration of the slumping (constant-velocity) phase, $\tilde{t}_{sp}$, the maximum front velocity is considered the beginning of the slumping stage, and a 10 % decay from the maximum velocity marks its end. The inset of figure 5(*b*) shows the relationship between the duration of the slumping stage and the time scale ratio $\tilde{S}$. Initially, the front velocity of the current undergoes a brief acceleration, followed by a slight decrease or near-constant phase ($\tilde{u}_{front}\approx 0.6$), and finally decelerates. It is consistent with the typical comprehension of the lock-exchange gravity current (Huppert & Simpson 1980; Cantero *et al.* 2007; Huang *et al.* 2008). Before $\tilde{t}=12$, the simulated results of gravity current are quantitatively consistent with the experimental results and numerical results reported in previous studies (Necker *et al.* 2002; Dai 2014; Gadal *et al.* 2023). For the saline flow front, the simulated results at $\tilde{t}<15$ are quite consistent with the previous results (Necker *et al.* 2002; Dai 2014). At $\tilde{t}>15$, the difference in simulation comes from the limitation of the streamwise length of the computational domain. For particle flow, the decrease of ξ_{sp} corresponds to the enhancement of the particle settling effect, indicated by an increase in $\tilde{S}$. This results in the front leaving the constant-velocity slumping stage earlier, which is consistent with previous observations (Gladstone & Woods 2000; Gadal *et al.* 2023). The front position for $\tilde{S}=0.033$ simulated in this work is basically enveloped by the front curves of $\tilde{S}=0.076$ and $\tilde{S}=0.026$ from Gadal *et al.* (2023). All of the above show that our simulation results have good credibility.

The salinity distribution and the particle dataset yield similar front position and velocity values in the dual-driven current, showing minimal differences. This suggests a high degree of coordination between salinity and particle diffusion and propagation under strong fluid–particle interactions. During the acceleration stage, the front velocity in

https://doi.org/10.1017/jfm.2025.10393 Published online by Cambridge University Press

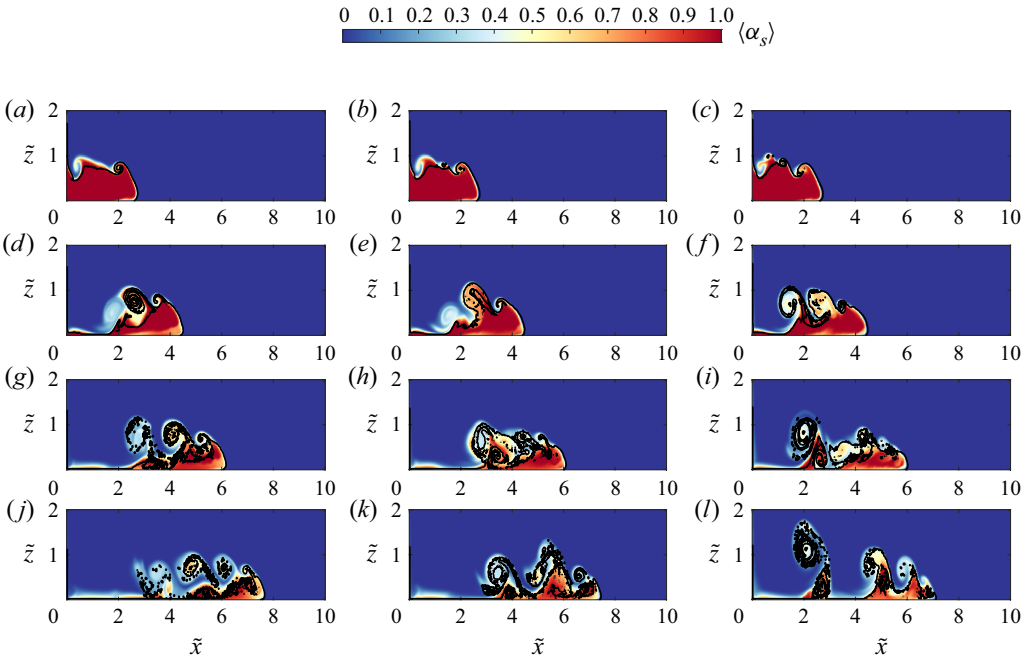


Figure 6. Spatial distribution of spanwise-averaged relative volume fraction of saline fluid $\langle\alpha_s\rangle$ and particle flow profile. The heat map shows the relative volume fraction of the saline fluid, and the black line indicates the outer contour of the particle flow. Here (*a*,*d*,*g*,*j*) $\xi_{sp} = 6.0$, (*b*,*e*,*h*,*k*) $\xi_{sp} = 1.0$ and (*c*,*f*,*i*,*l*) $\xi_{sp} = 0.17$; (*a*–*c*) $\tilde{t} = 3$, (*d*–*f*) $\tilde{t} = 6$, (*g*–*i*) $\tilde{t} = 9$ and (*j*–*l*) $\tilde{t} = 12$.

figure 5(*b*) is independent of ξ_{sp}, consistent with the findings in Gladstone & Woods (2000). The duration of the slumping stage ($\tilde{t}_{sp}$) is gradually shortened as $\tilde{S}$ increases corresponding to a decrease in ξ_{sp}. The reason for the short slumping stage at large ξ_{sp} is that the low particle settling velocity enhances the backflow's propagation (Huang *et al.* 2008), enabling the reflected wave to catch up with the front more quickly and alter the front dynamics. When ξ_{sp} is small, the stronger particle settling effect is primarily responsible for the earlier end time of the slumping stage.

The salinity and particle distribution of the dual-driven current at various ξ_{sp}s are depicted in figure 6. It can be seen that the salinity propagation is closely connected to the particle movement in the dual-driven current. A reduction in ξ_{sp}, which decreases the interstitial fluid density and thereby increases particle settling, results in a slower advancement velocity, reduced ability to maintain head shape (Huang *et al.* 2008) and a lower relative saline fluid fraction α_s near the head. Compared with the salinity-dominated current (figure 6*a*), the particle-dominated current (figure 6*c*) is more prone to interfacial instability at early stages, leading to the formation of KH billows. The interfacial instability structures in the salinity-dominated current (figure 6*a*,*d*,*g*,*j*) are generally confined to the region where $\tilde{z} < 1$. The excited interfacial vortex propagates downstream with the current, rapidly expands in size, and then slowly dissipates as salinity diffuses. In contrast, the interfacial vortex in particle-dominated current essentially does not move streamwise (figure 6*f*,*i*,*l*). The vortex continues to grow spatially throughout the evolution. Such pronounced vortices have also been reported in previous studies on PD gravity currents (Nasr-Azadani & Meiburg 2014; Lu *et al.* 2024). These vortices form due to the interaction between wall-reflected bores and vortices induced by the settling of particle groups. As the strength of vortex structure progressively weakens, the reduced fluid forces are

https://doi.org/10.1017/jfm.2025.10393 Published online by Cambridge University Press

insufficient to retain the particles within the vortex, especially at small ξ_{sp}. Thus, particles are displaced by centrifugal force, leading to an expansion in the vortex's spatial range.

From the above analysis, the key phenomena and transition regimes from SD to PD current can be summarized as follows.

(i) Material transport: analysing the variations in transport capacity for salinity and particles is crucial for comprehending SPDD current behaviour.
(ii) Interfacial instability: this phenomenon is linked to the entrainment regime and thus the density dilution of interstitial fluid, significantly altering current dynamics.

3.2. *Salinity convection–diffusion and particle transport*

The material transport capacity can be reflected by the equivalent material height $\tilde{h}$ and current height $\tilde{h}_t$ which includes the transporting material covering transported particle part $\tilde{h}_{p,t}$ and saline fluid part $\tilde{h}_s$. The difference between the two is that the latter isolates the contribution of the deposited particles $\tilde{h}_{p,d}$, yielding $\tilde{h} = \tilde{h}_t + \tilde{h}_{p,d} = (\tilde{h}_{p,t} + \tilde{h}_s) + \tilde{h}_{p,d}$. The equivalent material height $\tilde{h}$ can be given by referring to Cantero *et al.* (2007, 2008), Shin, Dalziel & Linden (2004) and Birman, Martin & Meiburg (2005) as

$$\tilde{h} = \int_0^{\tilde{L}_z} \langle \tilde{\rho}_m \rangle \mathrm{d}\tilde{z} = \int_0^{\tilde{L}_z} \frac{\langle \alpha_p \rangle \left(\rho_p - \rho_w\right)}{\rho_{m0} - \rho_w} \mathrm{d}\tilde{z} + \int_0^{\tilde{L}_z} \frac{\langle \alpha_f \rangle (\langle \alpha_s \rangle \rho_s + \langle \alpha_w \rangle \rho_w - \rho_w)}{\rho_{m0} - \rho_w} \mathrm{d}\tilde{z}. \tag{3.1}$$

The first and second terms on the right-hand side represent the height contributed from particles and salinity denoted as $\tilde{h}_p = \tilde{h}_{p,t} + \tilde{h}_{p,d}$ and $\tilde{h}_s$, respectively. The deposited particle height $\tilde{h}_{p,d}$ is calculated by

$$\tilde{h}_{p,d} = \frac{\rho_p - \rho_w}{\rho_{m0} - \rho_w} \int_0^{\tilde{L}_z} \langle \alpha_{p,d} \rangle \mathrm{d}\tilde{z}, \tag{3.2}$$

where $\langle \alpha_{p,d} \rangle$ denotes the spanwise-averaged volume fraction of deposited particles, which is given by

$$\langle \alpha_{p,d}(x) \rangle = N^l_{p,d}(x) V_p N_x / L_x L_y, \tag{3.3}$$

in which $N^l_{p,d}(x)$ is the deposited particle number in the region $\mathcal{R} = (x - (L_x/2N_x), x + (L_x/2N_x))$. The deposited particles here refer to the particles that are in contact with the bottom wall and have a velocity $|\tilde{\boldsymbol{u}}_p|$ less than 10^{-2}. It is important to note that both the equivalent material height $\tilde{h}$ and current height $\tilde{h}_t$ account for the material transported by large-sized vortices in the flow field, aligning with the approach in previous studies (Cantero *et al.* 2007, 2008). This is primarily because these vortices are a significant feature generated by the current and exert a non-negligible influence on its dynamics.

Figure 7 illustrates the spatiotemporal evolution of three material heights ($\tilde{h}_s/\tilde{h}$, $\tilde{h}_p/\tilde{h}$ and $\tilde{h}$) at varying ξ_{sp}s. Regions with locally large salinity height $\tilde{h}_s$ often corresponds to regions with locally large $\tilde{h}$, indicating that the interstitial fluid is essential to the material transport. The relative salinity/particle height ($\tilde{h}_s/\tilde{h}$, $\tilde{h}_p/\tilde{h}$) in the head essentially stays constant in the slumping stage. It suggests that the composition ratio of salinity to particle in the head region remains in equilibrium. This balance is crucial for maintaining the constant front velocity regime of the slumping stage. During the slumping stage, the equivalent material height $\tilde{h}$ near the head is approximately unity, which corresponds to half the initial height of the fluid–particle column. This observation aligns with previous studies (Necker *et al.* 2002; Cantero *et al.* 2007; Bonometti & Balachandar 2008; Meiburg

https://doi.org/10.1017/jfm.2025.10393 Published online by Cambridge University Press

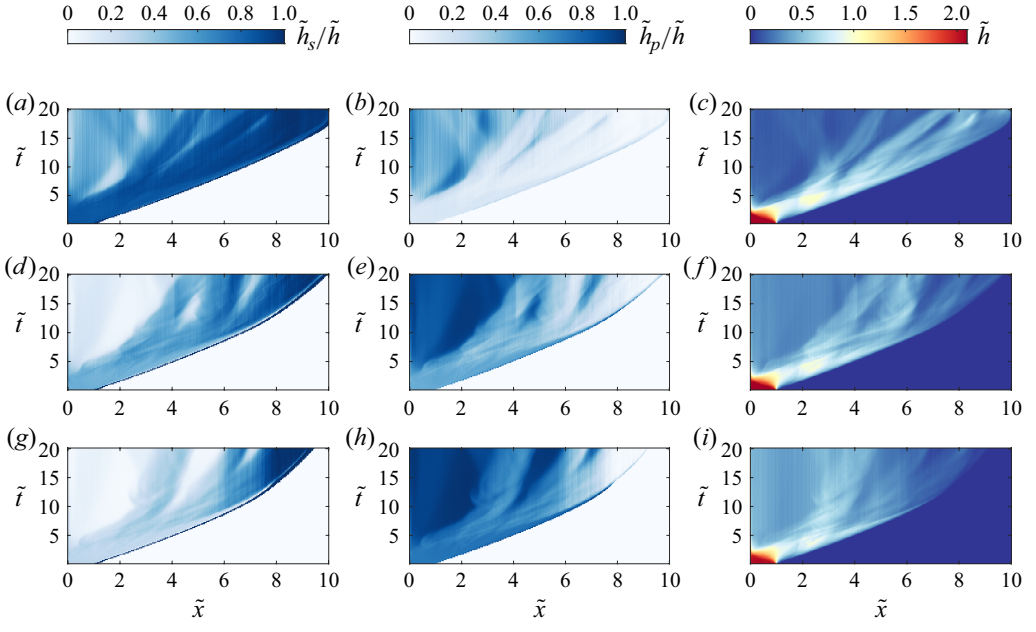


Figure 7. Spatiotemporal evolution of material heights for various cases: (*a–c*) $\xi_{sp} = 6.0$, (*d–f*) $\xi_{sp} = 1.0$ and (*g–i*) $\xi_{sp} = 0.17$; (*a*,*d*,*g*) relative salinity height $\tilde{h}_s/\tilde{h}$, (*b*,*e*,*h*) relative particle height $\tilde{h}_p/\tilde{h}$ and (*c*,*f*,*i*) equivalent material height $\tilde{h}$.

et al. 2015). The position of the maximum $\tilde{h}$ progressively shifts away from the head as ξ_{sp} decreases after entering the deceleration period (approximately $\tilde{t} > 10$) in figure 7(*c*,*f*,*i*). When ξ_{sp} is small, the inherent sedimentation properties of the particles cause the density difference between the gravity current and the ambient fluid to decay more. It corresponds to a faster decay of the forward ability (also see in figure 5), making it increasingly difficult for the particles to be transported downstream by the current.

We then discuss the ratio of transporting particles to deposited particles at different locations. Figure 8 illustrates the ratio of transporting particle height relative to total particle height, $\tilde{h}_{p,t}/\tilde{h}_p$, at different times and varying values of ξ_{sp}. During the slumping stage, ξ_{sp} has minimal influence on the ratio of transporting particle height, indicating that particle transport capacity and sedimentation are largely independent of ξ_{sp}. In this phase, the maximum $\tilde{h}_{p,t}/\tilde{h}_p$ near the front remains at unity, meaning the particles here are primarily transported in suspension. Particles in the upstream gradually settle, leading to a decrease in $\tilde{h}_{p,t}/\tilde{h}_p$. In the deceleration stage, gravity currents with larger ξ_{sp} exhibit higher $\tilde{h}_{p,t}/\tilde{h}_p$ values, particularly in terms of maximum $\tilde{h}_{p,t}/\tilde{h}_p$ near the front. This implies a great capacity of particle suspension at larger ξ_{sp}, corresponding to the greater forward velocity observed in figure 5. Upstream, after the current passes, $\tilde{h}_{p,t}/\tilde{h}_p$ stabilizes at approximately 0.3, indicating that most particles are deposited. This low $\tilde{h}_{p,t}/\tilde{h}_p$ results from the movement of particles within the near-wall region under the influence of residual flow.

Figure 9 depicts the spatiotemporal evolution of the proportions of transporting particle height ($\tilde{h}_{p,t}$) and salinity height ($\tilde{h}_s$) in the current height ($\tilde{h}_t$), and the evolution of the current height ($\tilde{h}_t$). The distribution patterns are qualitatively similar to those in figure 7. At larger ξ_{sp}, the particle effect on the current is weak, resulting in heights in figure 9(*a–c*)

https://doi.org/10.1017/jfm.2025.10393 Published online by Cambridge University Press

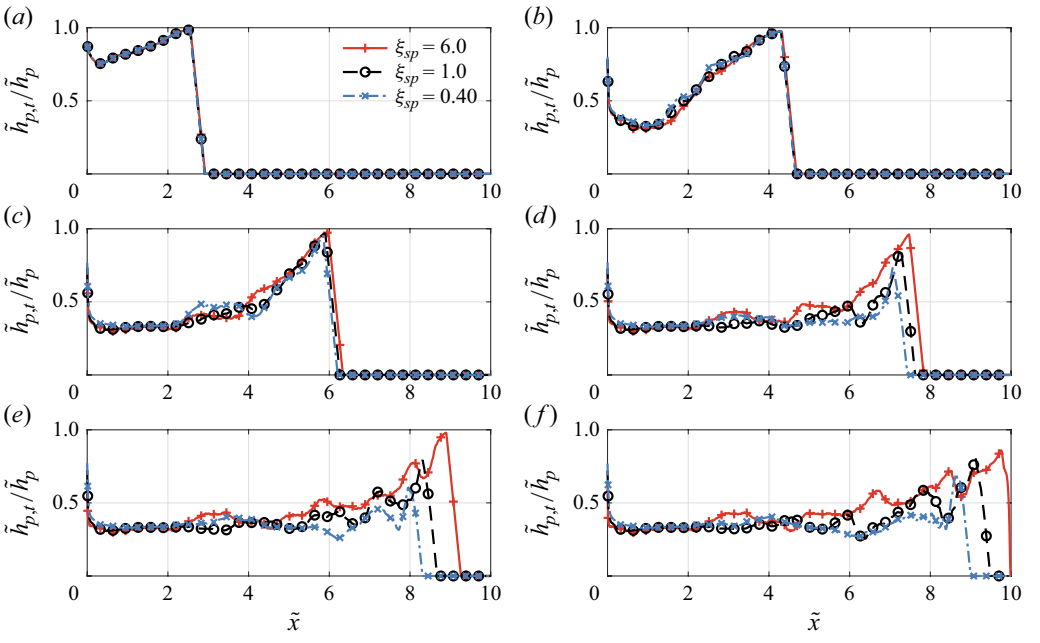


Figure 8. Spatial distribution of the ratio of transporting particle height to particle height $\tilde{h}_{p,t}/\tilde{h}_p$: (*a*) $\tilde{t} = 3$, (*b*) $\tilde{t} = 6$, (*c*) $\tilde{t} = 9$, (*d*) $\tilde{t} = 12$, (*e*) $\tilde{t} = 15$ and (*f*) $\tilde{t} = 18$.

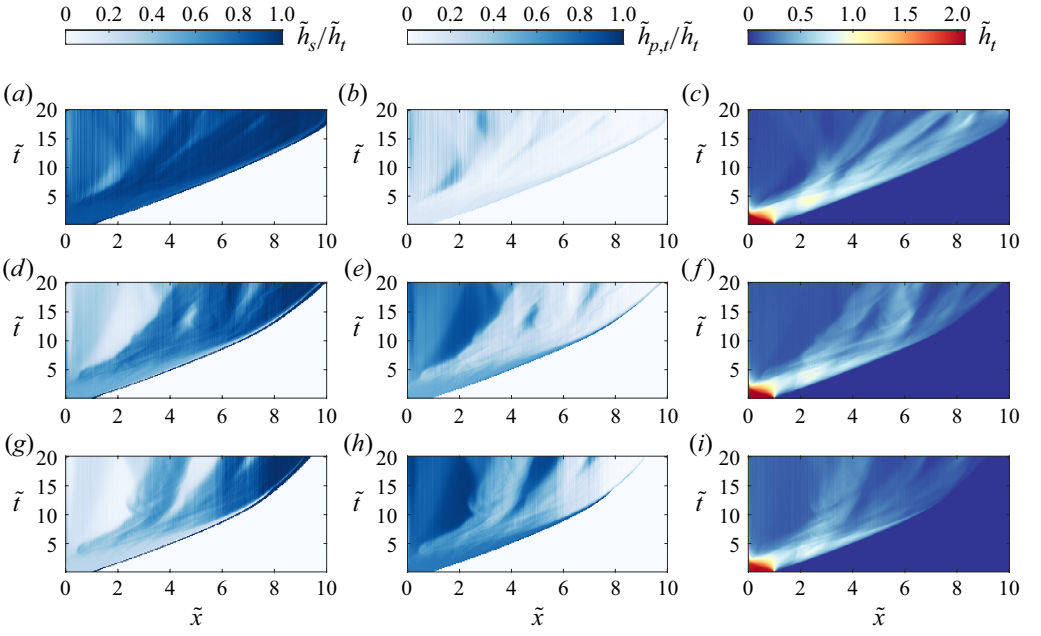


Figure 9. Spatiotemporal evolution of current heights for various cases: (*a–c*) $\xi_{sp} = 6.0$, (*d–f*) $\xi_{sp} = 1.0$ and (*g–i*) $\xi_{sp} = 0.17$; (*a*,*d*,*g*) relative salinity height $\tilde{h}_s/\tilde{h}_t$, (*b*,*e*,*h*) relative transporting particle height $\tilde{h}_{p,t}/\tilde{h}_t$ and (*c*,*f*,*i*) current height $\tilde{h}_t$.

https://doi.org/10.1017/jfm.2025.10393 Published online by Cambridge University Press

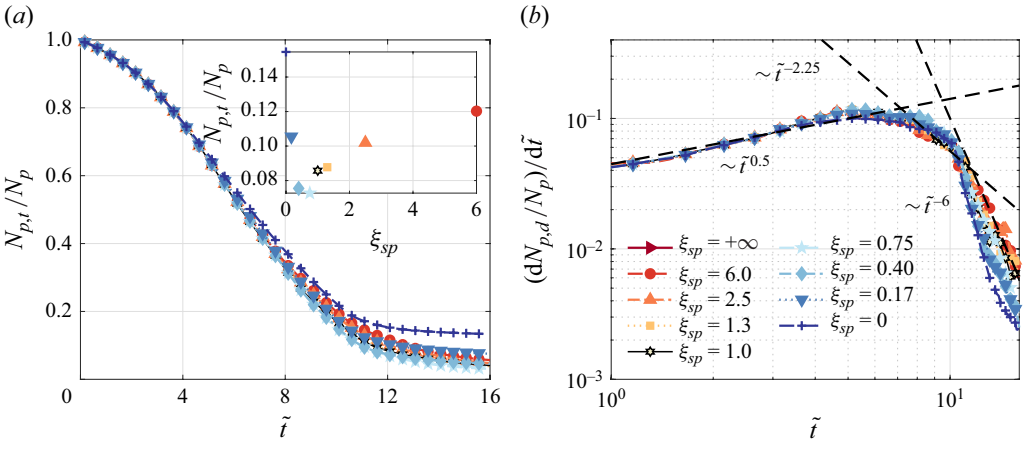


Figure 10. Time evolution of (*a*) transporting particle quantity $N_{p,t}$ and (*b*) particle deposition rate $\mathrm{d}N_{p,d}/\mathrm{d}\tilde{t}$, both of which are normalized by the total particle quantity N_p. The inset in panel (*a*) shows the transporting particle quantity at varying ξ_{sp}s at $\tilde{t}=12$.

comparable to the heights observed in figure 7(*a–c*). Conversely, when ξ_{sp} is small, particle deposition reduces transporting material heights by $\tilde{h}_{p,d}$, causing the values in figure 9(*h–i*) to be lower than those in figure 7(*h–i*).

A statistical analysis of the number of deposited particles is crucial for understanding the deposition process in gravity current. Figure 10 illustrates the time evolution of normalized transporting particle number $N_{p,t}/N_p$ and the corresponding deposition rate $\mathrm{d}(N_{p,d}/N_p)/\mathrm{d}\tilde{t}$ under different values of ξ_{sp}. During the early stage of the current ($\tilde{t}<10$), the deposition process is independent of ξ_{sp}, and the deposition rate scales with $\tilde{t}^{\,0.5}$, which is consistent with previous findings (Necker *et al.* 2002; Espath *et al.* 2014; Francisco *et al.* 2017). As the current experiences a short stage ($8<\tilde{t}<10$) developing from the slumping stage to the deceleration stage, the deposition rate decreases following a scaling law of $\tilde{t}^{-2.25}$. For $\tilde{t}>10$, a decrease in ξ_{sp} leads to a lower deposition rate. It is attributed to the large-sized vortex structures in the flow field (Necker *et al.* 2002) as seen in figure 6, which trap some particles and hinder sedimentation. This phenomenon is evident from the higher number of transporting particles at very small ξ_{sp}, as shown in the inset of figure 10(*a*). At this stage, the deposition rate scales approximately with $\tilde{t}^{-6}$, slightly higher than the earlier decay rate (Necker *et al.* 2002; Espath *et al.* 2015). This difference is attributed to the higher particle settling velocity $\tilde{\gamma}_t$ in this study (Necker *et al.* 2005; Espath *et al.* 2015; Francisco *et al.* 2017).

We compute the average vertical predominant forces ($\tilde{\boldsymbol{F}}_z^{\nabla p}$, $\tilde{\boldsymbol{F}}_z^{d}$, and $\tilde{\boldsymbol{F}}_z^{c}$) acting on the transported particles (Xie *et al.* 2023*a*) to elucidate the effect of salinity–particle interaction on particle suspension, as illustrated in figure 11. Changes in ξ_{sp} have a minimal effect on the dominant drag force (figure 11*a*) and pressure gradient forces (figure 11*b*) before the slumping stage. At this stage, the primary pressure gradient force initially rises and then falls, while the secondary drag force mostly stays constant. After that, both ($\tilde{\boldsymbol{F}}_z^{\nabla p}$ and $\tilde{\boldsymbol{F}}_z^{d}$) gradually diminish. As the particle concentration increases, the contact force takes on greater significance in maintaining particle suspension (figure 11*c*). With ξ_{sp} decreasing, and given that the dimensionless deposition rates are comparable (figure 10), a larger number of particles are deposited, further reducing the mixture density of the gravity current. This reduction in density weakens the flow dynamics, significantly

https://doi.org/10.1017/jfm.2025.10393 Published online by Cambridge University Press

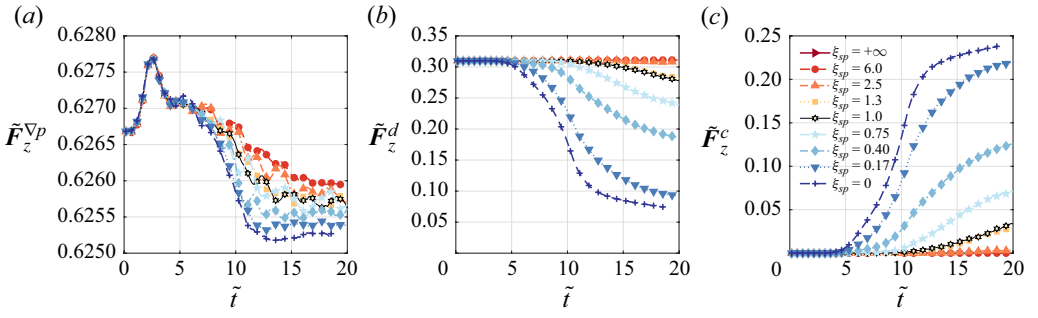


Figure 11. Average vertical forces acting on transported particles over time. (*a*) Pressure gradient force $\tilde{\boldsymbol{F}}_z^{\nabla p}$, (*b*) drag force $\tilde{\boldsymbol{F}}_z^{d}$ and (*c*) contact force $\tilde{\boldsymbol{F}}_z^{c}$.

	Case 1	Case 2	Case 3	Case 4	Case 5	Case 6	Case 7	Case 8	Case 9
$\tilde{h}_t$ [–]	0.6666	0.6558	0.6431	0.6429	0.6408	0.6340	0.6281	0.6132	0.6088

Table 2. Average current interface elevations over $\tilde{x} = 1.4{-}1.8$ at $\tilde{t} = 2.5$.

decreasing the pressure gradient force and drag force, as shown in figure 11(*a*,*b*). Consequently, the particle suspension ability declines and the particle settling is enhanced, as illustrated in figure 8. Additionally, with particles gradually settling, the increased particle concentration near the wall leads to a corresponding rise in the contact force, as depicted in figure 11(*c*).

3.3. *Entrainment and detrainment*

One of the key mechanisms to entrainment is the formation of a series of billows resulting from interfacial shear instability, which alters the density difference with the ambient fluid by affecting the material concentration of the current (Wells & Dorrell 2021). Here we focus on current entrainment during the slumping phase characterized by a constant velocity. Figure 12(*a–f*) displays the spanwise-averaged flow profiles averaged over $\tilde{x} = 1.4{\sim}1.8$ at $\tilde{t} = 2.5$ (in the slumping stage), including fluid streamwise velocity $\langle\tilde{u}_f\rangle$, fluid vertical velocity $\langle\tilde{w}_f\rangle$, fluid density $\langle\tilde{\rho}_f\rangle$, relative particle volume fraction $\langle\alpha_p\rangle/\alpha_{p0}$, mixture density $\langle\tilde{\rho}_m\rangle$ and gradient Richardson number $\langle Ri_g\rangle$. The spatial distribution of the vertical total force $\boldsymbol{F}_z^T$ on the particles in the slumping stage for various cases is shown in figure 12(*g–i*).

For the sake of interface definition, the current height $\tilde{h}_t$ is considered as the interface elevation. The average interface elevations over $\tilde{x} = 1.4{\sim}1.8$ at $\tilde{t} = 2.5$ are presented in table 2. The downward sedimentation of particles inevitably causes the current interface to descend, and the degree of descent increases with the decrease of ξ_{sp}. With regard to $\langle\tilde{u}_f\rangle$ profiles (figure 12*a*), the decrease of ξ_{sp} reduces $\langle\tilde{u}_f\rangle$ at the interface but increases $\partial\langle\tilde{u}_f\rangle/\partial\tilde{z}$ here. It increases $\langle\tilde{u}_f\rangle$ below the interface, which is consistent with the results of Shringarpure *et al.* (2015). Figure 12(*b*) illustrates that, in most regions (excluding the range $\tilde{z} = 0.4{\sim}0.7$), a decrease in ξ_{sp} results in a leftward shift of the $\langle\tilde{w}_f\rangle$ profile. This shift indicates a reduction in upward vertical velocity (at $\tilde{z} \gtrapprox 0.7$ and the very near the wall as shown in the inset) and an increase in downward vertical velocity (at $\tilde{z} \lessapprox 0.4$). This phenomenon is closely associated with particle sedimentation.

https://doi.org/10.1017/jfm.2025.10393 Published online by Cambridge University Press

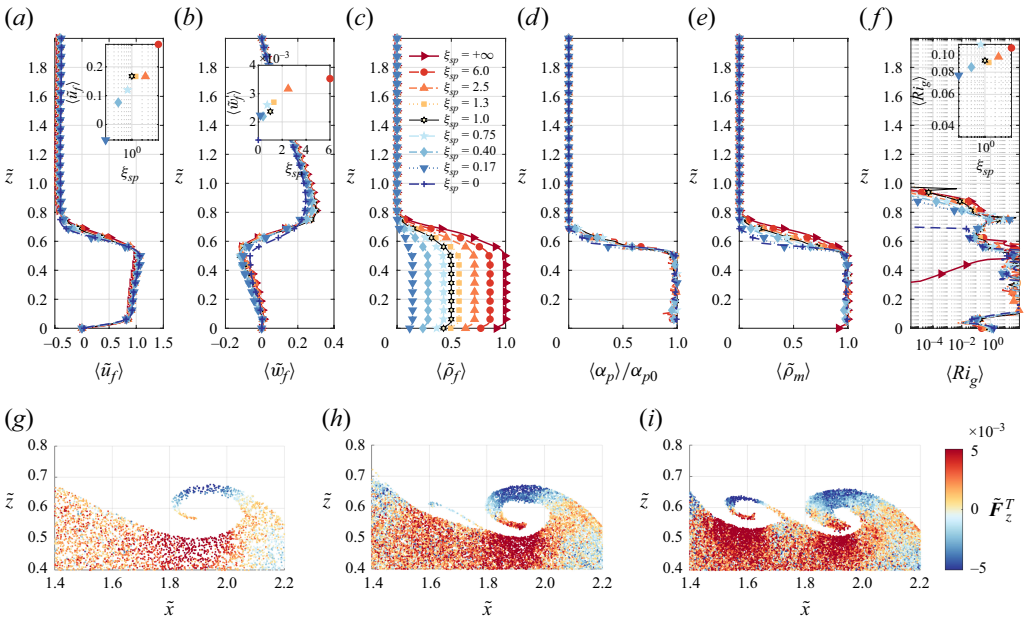


Figure 12. Spanwise-averaged current profiles at $\tilde{t} = 2.5$ averaged over $\tilde{x} = 1.4{\sim}1.8$: (*a*) fluid streamwise velocity $\langle\tilde{u}_f\rangle$; (*b*) fluid vertical velocity $\langle\tilde{w}_f\rangle$; (*c*) fluid density $\langle\tilde{\rho}_f\rangle$; (*d*) relative particle volume fraction $\langle\alpha_p\rangle/\alpha_{p0}$; (*e*) mixture density $\langle\tilde{\rho}_m\rangle$; (*f*) gradient Richardson number $\langle Ri_g\rangle$. The insets in panels (*a*) and (*f*) plot $\langle\tilde{u}_f\rangle$ and $\langle Ri_g\rangle$, respectively, at current height $\tilde{h}_t$ which is given in table 2 at different ξ_{sp}. The inset in panel (*b*) shows the relationship between mean fluid vertical velocity $\langle\tilde{w}_f\rangle$ near the wall ($\tilde{z} = 0{\sim}0.05$) and ξ_{sp}. Spatial distribution of vertical total force $\tilde{\boldsymbol{F}}_z^T$ acting on particles at $\tilde{t} = 2.5$ for (*g*) $\xi_{sp} = 6.0$, (*h*) $\xi_{sp} = 1.0$ and (*i*) $\xi_{sp} = 0.17$. The higher density of the granular medium arises from the projection of three-dimensional Lagrangian particle points onto a two-dimensional plane.

Conversely, within the range $\tilde{z} = 0.4{\sim}0.7$, smaller ξ_{sp} values cause the profile to shift to the right, a behaviour attributed to enhanced interface instability. Simultaneously, the interface fluid stratification is reduced with ξ_{sp} decreasing, as evidenced by the decrease in $\partial\langle\tilde{\rho}_f\rangle/\partial\tilde{z}$ in figure 12(*c*), and the fluid–particle mixture stratification also diminishes (figure 12*e*) under the impact of the particle spatial distribution. Additionally, as shown in figure 12(*f*), Ri_g near the interface is positively correlated with ξ_{sp} and clearly falls below the classical shear instability threshold of 1/4 (Nasr-Azadani *et al.* 2018; Caulfield 2021). This explains why, during the slumping stage, currents with low ξ_{sp} are more prone to become unstable and form interfacial billows. Correspondingly, the particles in the low-ξ_{sp} regime are more easily rolled up by the stronger fluid forces provided by the vortices as shown in figure 12(*g–i*).

By setting thresholds on the volume fraction to capture the envelope ($\langle\alpha_s\rangle = 10^{-3}$ and $\langle\alpha_p\rangle/\alpha_{p0} = 10^{-2}$) which is similar to He *et al.* (2018), we determine the corresponding current volumes per unit width, $\tilde{V}_{F,s}$ and $\tilde{V}_{F,p}$. Then, we can get the current volume change rate per unit width by $\tilde{Q}_{F,s(p)} = \mathrm{d}\tilde{V}_{F,s(p)}/\mathrm{d}\tilde{t}$. The entrainment velocity ($\tilde{W}_{s(p)}$) and entrainment coefficient ($\tilde{\mathcal{E}}_{s(p)}$) can be given by (Ottolenghi *et al.* 2016)

$$\tilde{W}_{s(p)} = \frac{\tilde{Q}_{F,s(p)}}{\tilde{L}_{F,s(p)}}, \quad \tilde{\mathcal{E}}_{s(p)} = \frac{\tilde{W}_{s(p)}}{\tilde{u}_{front,s(p)}}, \tag{3.4}$$

https://doi.org/10.1017/jfm.2025.10393 Published online by Cambridge University Press

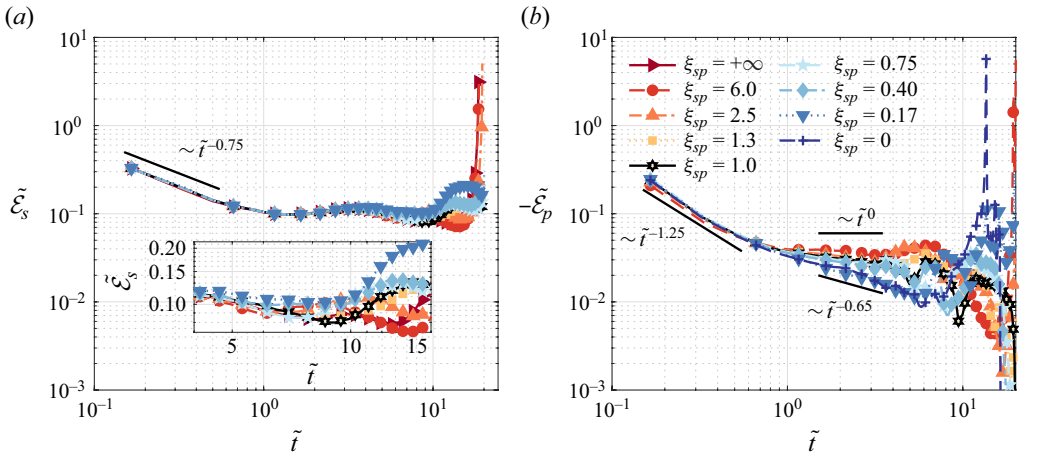


Figure 13. Time evolution of entrainment coefficients for (*a*) saline flow $\tilde{\mathcal{E}}_s$ and (*b*) particle flow $\tilde{\mathcal{E}}_p$.

where $\tilde{L}_{F,s(p)}$ denotes the length of the upper interface. Given that the deposited particles form only a very thin layer and often coexist in thin layers with near-wall moving particles, their inclusion in the interface identification using volume fraction has a negligible effect on the captured volume and can therefore be ignored. Figure 13 depicts the time evolution of entrainment coefficients ($\tilde{\mathcal{E}}_{s(p)}$). The entrainment coefficients for particle flow and saline flow are distinct: $\tilde{\mathcal{E}}_s > 0$ in figure 13(*a*) and $\tilde{\mathcal{E}}_p < 0$ in figure 13(*b*), respectively. This indicates that the saline flow is always entraining the fluid, while the particle flow is always detraining the fluid due to particle gravity. Here $\tilde{\mathcal{E}}_s > |\tilde{\mathcal{E}}_p|$, meaning that in the dual-driven current, the entrainment from salinity convection–diffusion is always greater than the detrainment from particle flow sedimentation. Both $\tilde{\mathcal{E}}_s$ and $\tilde{\mathcal{E}}_p$ undergo the initial fast decay, governed by complex vertical and horizontal dynamics. After that (in the slumping stage), $\tilde{\mathcal{E}}_{s(p)}$ decreases slightly or stabilizes, aligning with He *et al.* (2018). Finally, $\tilde{\mathcal{E}}_{s(p)}$ at large ξ_{sp} exhibits a significant rise as a result of impact on the downstream wall. The entrainment/detrainment of saline/particle flow is independent of ξ_{sp} in the early stage ($\tilde{t} < 1$), with $\tilde{\mathcal{E}}_s$ decaying faster ($\sim\tilde{t}^{-1.25}$) than $\tilde{\mathcal{E}}_p$ ($\sim\tilde{t}^{-0.75}$). Then, the particle sedimentation effect impacts both entrainment and detrainment. The entrainment coefficient of saline flow is approximately 0.1 as close to the previous reports (Van den Bremer & Hunt 2014; He *et al.* 2018; Parker *et al.* 2020; Richardson & Hunt 2022; Salizzoni *et al.* 2024), and is facilitated by the decrease in ξ_{sp}, particularly during the deceleration phase. This is because the presence of particles promotes interface instability in figure 6. This explains also why, as ξ_{sp} decreases, the particle flow detrainment weakens. In the slumping stage, when $\xi_{sp} = 0$, $\tilde{\mathcal{E}}_p$ decays at a rate of $\tilde{t}^{-0.05}$, whereas $\tilde{\mathcal{E}}_p$ is essentially constant when $\xi_{sp} = 6.0$. The high-ξ_{sp} flow exhibits a weaker detrainment during the deceleration period (figure 13*b*), primarily because the interfacial vortices are continuously excited (figure 6).

Figure 14 illustrates the time evolution of the entrainment and detrainment coefficients ($\tilde{\mathcal{E}}_s$ and $\tilde{\mathcal{E}}_p$) under different current interface definition thresholds ($\langle\alpha_s\rangle$ for saline flow and $\langle\alpha_p\rangle/\alpha_{p0}$ for particle flow). Within the range of $\langle\alpha_s\rangle$ and $\langle\alpha_p\rangle/\alpha_{p0}$ values shown in the figure, changes in the threshold values do not qualitatively alter the temporal trends of $\tilde{\mathcal{E}}_s$ and $\tilde{\mathcal{E}}_p$. Specifically, increasing the $\langle\alpha_s\rangle$ threshold slightly reduces the entrainment coefficient, while increasing the $\langle\alpha_p\rangle/\alpha_{p0}$ threshold slightly enhances the detrainment

https://doi.org/10.1017/jfm.2025.10393 Published online by Cambridge University Press

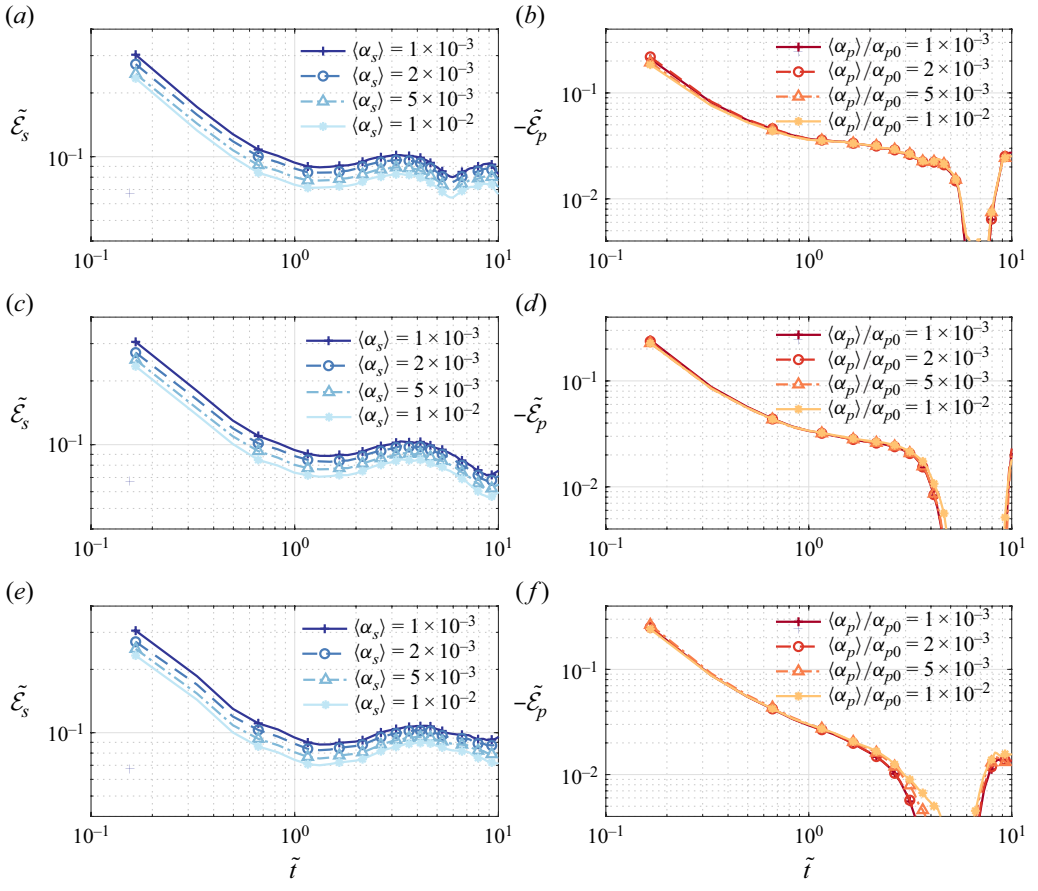


Figure 14. Time evolution of entrainment coefficients for (*a*,*c*,*e*) saline flow $\tilde{\mathcal{E}}_s$ and (*b*,*d*,*f*) particle flow $\tilde{\mathcal{E}}_p$ with different interface definition thresholds: (*a*,*b*) $\xi_{sp} = 6.0$, (*c*,*d*) $\xi_{sp} = 1.0$ and (*e*,*f*) $\xi_{sp} = 0.17$.

coefficient. This behaviour arises because larger threshold values encompass smaller captured current volumes. Considering that interface vortices can contain substantial amounts of matter and influence current dynamics below, we here treat vortices near the interface as part of the gravity current. Accordingly, adopting a relatively small threshold value captures most of the saline and particle flow contours, thereby providing a more comprehensive depiction of material entrainment and detrainment.

4. Conclusions and discussion

This work studies the lock-exchange SPDD gravity current using a DNS DEM numerical method. The flow Reynolds number is maintained at 2071. The transition regime of gravity current from SD to PD is investigated by introducing the variable ξ_{sp}, which represents the ratio of the salinity contribution and the particle contribution to the density difference.

The results indicate that the transition regime from SD gravity current to PD gravity current is related to interface dynamics and material transport behaviour. The interfacial stability during this transition is affected by a positive feedback loop between interstitial fluid entrainment and particle settling. As ξ_{sp} decreases, associated with the enhanced particle contributions, the intensity of interfacial fluid stratification and the gradient Richardson number decrease. This reduction increases the likelihood of the interfacial

https://doi.org/10.1017/jfm.2025.10393 Published online by Cambridge University Press

instability and KH billow formation. As a result, the formation of interfacial vortices accelerates fluid entrainment, leading to further dilution of the interstitial fluid, which, in turn, amplifies the particle settlement effect over time. During the slumping stage, stronger KH billows at large ξ_{sp} enhance the streamwise transport of particles (Xie, Hu & Pan 2025), while the sedimentation of more particles supplies more abundant energy to drive the current downstream. The synergistic effect of these processes enables the front velocity of the particle-dominated current to remain comparable to that of the salinity-dominated current, despite greater material loss and a corresponding reduction in density difference with the ambient fluid. In the later stage, the pursuit of wall-reflected bore and the deposition of more particles at large ξ_{sp} cause the front velocity to decay faster, making the current enter the deceleration stage.

Additionally, salinity and particles possess distinct diffusion and transport properties, with saline flow characterized by entrainment and particle flow by detrainment. This highlights that the spatial distribution of materials is significantly affected by ξ_{sp}, and the current ability of transporting particles gradually decreases with increasing particle contribution. As ξ_{sp} decreases, the reduction in particle flow detrainment is attributed to larger interfacial vortices. Over time, the wall-reflected bore combines with vortices generated by particle settling dynamics, forming a larger vortex structure. As the current weakens, the diminishing vortex strength causes particles to migrate away from the vortex centre due to centrifugal forces, resulting in the continuous spatial expansion of the vortex.

Future research can explore dual-driven gravity currents with higher Re, varying St and different particle settling velocities to gain a deeper comprehension of the entrainment–detrainment mechanism in the current.

Funding. The work was supported by the Postdoctoral Fellowship Program of CPSF (grant no. GZB20240656 for J.X.), the China Postdoctoral Science Foundation (grant no. 2024M752777 for J.X.) and the National Natural Science Foundation of China (grant no. 12222211 for D.P.).

Declaration of interests. The authors report no conflict of interest.

Data availability. The authors declare that all data supporting the findings of this study are available within the paper.

Appendix A. Validation of particles settling in linearly stratified environment

We examine the settling behaviour of a suspension of particles in a linearly stratified fluid environment to evaluate the model's capability in simulating the effects of particle sedimentation on fluid density mixing. The computational domain is a cubic region with dimensions of 0.02 m $\times$ 0.02 m $\times$ 0.02 m in length (L_x), width (L_y) and height (L_z). Periodic boundary conditions are applied in the streamwise (x) and spanwise (y) directions, and a no-slip wall boundary condition is enforced in the vertical (z) direction. The grid resolution is $N_x \times N_y \times N_z = 50 \times 50 \times 50$. The fluid kinematic viscosity is $\nu_f = 10^{-6}$ m^2 s^{-1}. By adjusting the volume ratio of fresh water to saline water, the fluid density ρ_f decreases linearly from the bottom to the top of the domain at the initial moment, following the relation

$$\rho_f = -\frac{\Delta\rho_f}{L_z}(z - L_z) + \rho_a, \tag{A1}$$

where $\Delta\rho_f = 20$ kg m^{-3} is the density difference between the top and bottom interfaces, and $\rho_a = 1000$ kg m^{-3} is the fluid density at the top interface which is marked as the background fluid density. The natural frequency of oscillation in the stratified fluid, known

https://doi.org/10.1017/jfm.2025.10393 Published online by Cambridge University Press

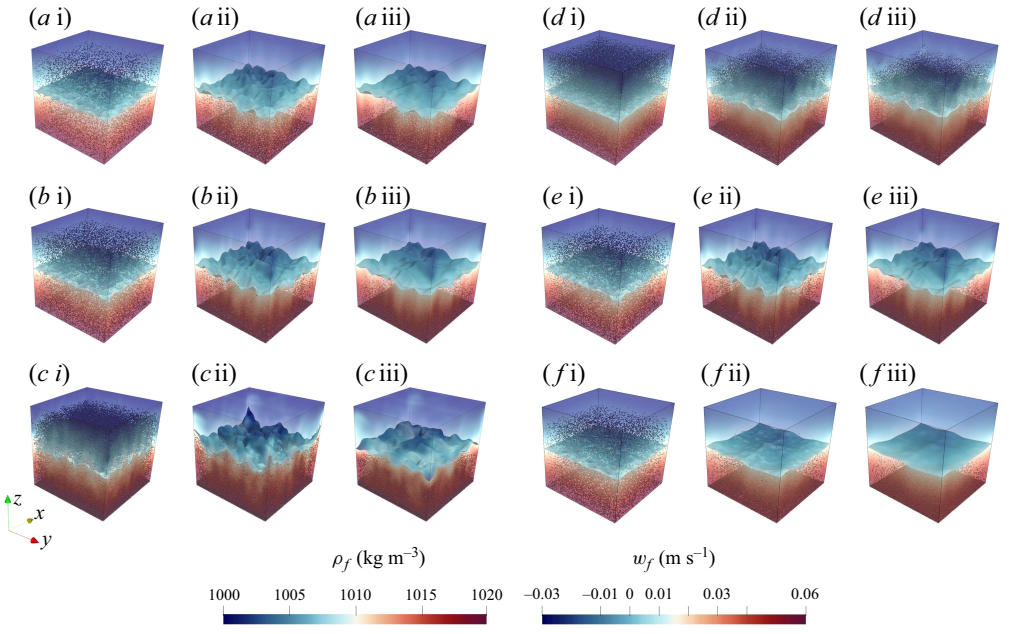


Figure 15. Snapshots of particles settling in the linearly stratified fluid at (*a*) $(\alpha_{p0}, Sc, d_p) = (0.5\,\%, 1, 0.2\,\text{mm})$, (*b*) $(\alpha_{p0}, Sc, d_p) = (1\,\%, 1, 0.2\,\text{mm})$, (*c*) $(\alpha_{p0}, Sc, d_p) = (5\,\%, 1, 0.2\,\text{mm})$, (*d*) $(\alpha_{p0}, Sc, d_p) = (1\,\%, 1, 0.1\,\text{mm})$, (*e*) $(\alpha_{p0}, Sc, d_p) = (1\,\%, 700, 0.2\,\text{mm})$ and (*f*) $(\alpha_{p0}, Sc, d_p) = (1\,\%, 0.1, 0.2\,\text{mm})$. In each panel, the three images from (i) to (iii) correspond to $t = 1/2N$, $t = 3/2N$ and $t = 2/N$. Each surface of the computational domain is coloured by the fluid density ρ_f. The isosurfaces within the flow field, defined by $\rho_f = 1010\ \text{kg m}^{-3}$, are coloured according to the fluid vertical velocity w_f. The spheres in the figure represent particles.

as the Brunt–Väisälä frequency $N = \sqrt{|\boldsymbol{g}|\Delta\rho_f/(\rho_a L_z)}$, is 3.13 s^{-1}. Initially, particles with zero velocity, a diameter of d_p and a density of $\rho_p = 2650\ \text{kg m}^{-3}$ are uniformly distributed throughout the computational domain. The bulk particle volume fraction is α_{p0}. The particle diameters d_p are 0.1 and 0.2 mm, with corresponding particle settling Reynolds numbers $Re_{p,t}$, as defined by (2.6), of approximately 0.9 and 7.2, respectively. The particle settling Froude number, $Fr = u_t/\sqrt{|\boldsymbol{g}|L_z\Delta\rho_f/\rho_a}$, representing the ratio of inertial to buoyancy time scales, is approximately 0.14 and 0.57, respectively. The bulk particle volume fraction α_{p0} is set to 0.5 %, 1 %, 5 %, and Schmidt number Sc is set to 0.1, 0.5, 1 and 700. After the simulation begins, the particles settle in the linearly stratified fluid due to gravity.

Figure 15 depicts the settling process of particles in a linearly stratified fluid under different conditions. Figure 16 illustrates the time evolution of the isosurface elevation variance $(\text{Var}(z/L_z))$ for a fluid density of $\rho_f = 1010\ \text{kg m}^{-3}$, alongside the fluid density profiles at $t = 4/N$ across varying conditions. As shown in figure 15, particle sedimentation induces the downward movement of the lower-density fluid with the density isopycnals distorted downward (Doostmohammadi & Ardekani 2015; Deepwell & Sutherland 2022), leading to fluctuations at the density interface and promoting the mixing of fluids with different densities. Once sedimentation is nearly complete, the interface stabilizes under the influence of buoyancy. Such evolution aligns with previous understandings (Magnaudet & Mercier 2020; More & Ardekani 2023). Thus, the variance in figure 16(*a–c*) initially increases and then decreases. Notably, the density is not fully

https://doi.org/10.1017/jfm.2025.10393 Published online by Cambridge University Press

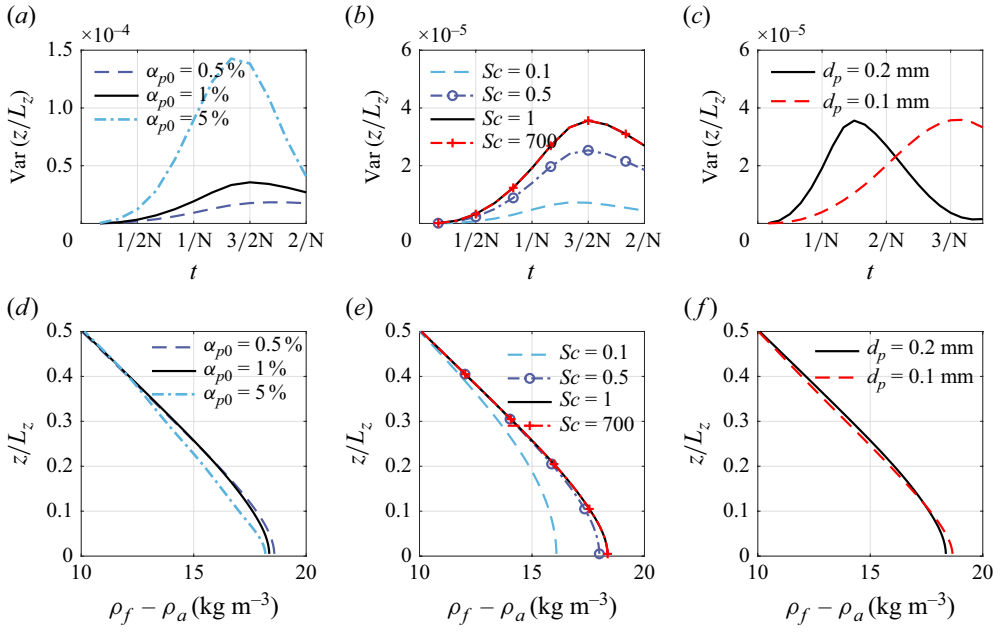


Figure 16. Comparison of mixing under (a,d) varying bulk particle volume fractions (α_{p0}), (b,e) varying Schmidt numbers (Sc) and (c,f) varying particle diameters (d_p). (a,b,c) Time evolution of the variance ($\mathrm{Var}(\bar{z}/L_z)$) of the elevation of the $\rho_f = 1010$ kg m^{-3} isosurface. (d,e,f) Average fluid density exceeding the background fluid density ($\rho_f - \rho_a$) at various elevations at $t = 4/N$.

mixed during particle setting, as the parameter $2\alpha_{p0}u_t/d_pN$ is less than 10, far below the mixing threshold of 60 proposed by Blanchette (2013).

As shown in figures 15(*a–c*) and 16(*a*), increasing particle volume fraction intensifies density interface instability. Higher α_{p0} correlates with lower density near the bottom (figure 16*d*), indicating enhanced fluid mixing. As the Schmidt number increases (the density diffusivity is weakened), although the fluid density isosurface perturbations intensify (figure 16*b*), the higher bottom fluid density (figure 16*e*) suggests reduced mixing. This is because low diffusivity (high Sc) reduces the ability to blur sharp interfaces while suppressing mixing, which increases variance. Notably, the impact of Sc increasing from 1 to 700 on the flow process is negligible. Larger particle sizes increase settling velocity, amplifying interface perturbations at $t < 3/2N$ as shown in figure 16(*c*) and enhancing fluid mixing as shown in figure 16(*f*). These insights into the effects of particle concentration, Schmidt number and particle size on the mixing process are consistent with Blanchette (2013). This demonstrates the model's ability to simulate the particle motion-induced fluid density mixing.

References

Arthur, R.S. & Fringer, O.B. 2014 The dynamics of breaking internal solitary waves on slopes. *J. Fluid Mech.* **761**, 360–398.

Balachandar, S. 2009 A scaling analysis for point–particle approaches to turbulent multiphase flows. *Intl J. Multiphase Flow* **35** (9), 801–810.

Birman, V.K., Martin, J.E. & Meiburg, E. 2005 The non-Boussinesq lock-exchange problem. Part 2. High-resolution simulations. *J. Fluid Mech.* **537**, 125–144.

Blanchette, F. 2013 Mixing and convection driven by particles settling in temperature-stratified ambients. *Intl J. Heat Mass Transfer* **56** (1-2), 732–740.

https://doi.org/10.1017/jfm.2025.10393 Published online by Cambridge University Press

BONNECAZE, R.T., HUPPERT, H.E. & LISTER, J.R. 1993 Particle-driven gravity currents. *J. Fluid Mech.* **250**, 339–369.

BONOMETTI, T. & BALACHANDAR, S. 2008 Effect of Schmidt number on the structure and propagation of density currents. *Theor. Comput. Fluid Dyn.* **22** (5), 341–361.

BÖTTNER, C., STEVENSON, C.J., ENGLERT, R., SCHÖNKE, M., PANDOLPHO, B.T., GEERSEN, J., FELDENS, P. & KRASTEL, S. 2024 Extreme erosion and bulking in a giant submarine gravity flow. *Sci. Adv.* **10** (34), eadp2584.

VAN DEN BREMER, T S. & HUNT, G R. 2014 Two-dimensional planar plumes and fountains. *J. Fluid Mech.* **750**, 210–244.

CANTERO, M.I., BALACHANDAR, S. & GARCÍA, M.H. 2008 An Eulerian–Eulerian model for gravity currents driven by inertial particles. *Intl J. Multiphase Flow* **34** (5), 484–501.

CANTERO, M.I., LEE, J.R., BALACHANDAR, S. & GARCIA, M.H. 2007 On the front velocity of gravity currents. *J. Fluid Mech.* **586**, 1–39.

CAULFIELD, C.P. 2021 Layering, instabilities, and mixing in turbulent stratified flows. *Annu. Rev. Fluid Mech.* **53** (1), 113–145.

CUNDALL, P.A. & STRACK, O.D.L. 1979 A discrete numerical model for granular assemblies. *Geotechnique* **29** (1), 47–65.

DAI, A. 2014 Non-Boussinesq gravity currents propagating on different bottom slopes. *J. Fluid Mech.* **741**, 658–680.

DEEPWELL, D. & SUTHERLAND, B.R. 2022 Cluster formation during particle settling in stratified fluid. *Phys. Rev. Fluids* **7** (1), 014302.

DOOSTMOHAMMADI, A. & ARDEKANI, A.M. 2015 Suspension of solid particles in a density stratified fluid. *Phys. Fluids* **27** (2), 023302.

ESPATH, L.F.R., PINTO, L.C., LAIZET, S. & SILVESTRINI, J.H. 2015 High-fidelity simulations of the lobe-and-cleft structures and the deposition map in particle-driven gravity currents. *Phys. Fluids* **27** (5), 056604.

ESPATH, L.F.R., PINTO, L.C., LAIZET, S. & SILVESTRINI, J.H. 2014 Two-and three-dimensional direct numerical simulation of particle-laden gravity currents. *Comput. Geosci.* **63**, 9–16.

FRANCISCO, E.P., ESPATH, L.F.R. & SILVESTRINI, J.H. 2017 Direct numerical simulation of bi-disperse particle-laden gravity currents in the channel configuration. *Appl. Math. Model.* **49**, 739–752.

GADAL, C., MERCIER, M.J., RASTELLO, M. & LACAZE, L. 2023 Slumping regime in lock-release turbidity currents. *J. Fluid Mech.* **974**, A4.

GLADSTONE, C. & WOODS, A.W. 2000 On the application of box models to particle-driven gravity currents. *J. Fluid Mech.* **416**, 187–195.

HÄRTEL, C., KLEISER, L., MICHAUD, M. & STEIN, C.F. 1997 A direct numerical simulation approach to the study of intrusion fronts. *J. Engng Maths* **32** (2/3), 103–120.

HÄRTEL, C., MEIBURG, E. & NECKER, F. 2000 Analysis and direct numerical simulation of the flow at a gravity-current head. Part 1. Flow topology and front speed for slip and no-slip boundaries. *J. Fluid Mech.* **418**, 189–212.

HE, Z., ZHAO, L., HU, P., YU, C. & LIN, Y.-T. 2018 Investigations of dynamic behaviors of lock-exchange turbidity currents down a slope based on direct numerical simulation. *Adv. Water Resour.* **119**, 164–177.

HE Z., ZHAO L., ZHU R. & HU P. 2019 Separation of particle-laden gravity currents down a slope in linearly stratified environments. *Phys. Fluids* **31** (10), 106602.

HUANG, H., IMRAN, J. & PIRMEZ, C. 2008 Numerical study of turbidity currents with sudden-release and sustained-inflow mechanisms. *J. Hydraul. Engng* **134** (9), 1199–1209.

HUPPERT, H.E. & SIMPSON, J.E. 1980 The slumping of gravity currents. *J. Fluid Mech.* **99** (4), 785–799.

JING, L., YANG, G.C., KWOK, C.Y. & SOBRAL, Y.D. 2019 Flow regimes and dynamic similarity of immersed granular collapse: a CFD-DEM investigation. *Powder Technol.* **345**, 532–543.

KNELLER, B., NASR-AZADANI, M.M., RADHAKRISHNAN, S. & MEIBURG, E. 2016 Long-range sediment transport in the world's oceans by stably stratified turbidity currents. *J. Geophys. Res.: Oceans* **121** (12), 8608–8620.

LU Y., LIU X., XIE X., SUN J., YANG Y. & GUO X. 2024 Particle-scale analysis on dynamic response of turbidity currents to sediment concentration and bedforms. *Phys. Fluids* **36** (3), 033316.

MAGNAUDET, J. & MERCIER, M.J. 2020 Particles, drops, and bubbles moving across sharp interfaces and stratified layers. *Annu. Rev. Fluid Mech.* **52** (1), 61–91.

MARSHALL, C.R., DORRELL, R.M., DUTTA, S., KEEVIL, G.M., PEAKALL, J. & TOBIAS, S.M. 2021 The effect of Schmidt number on gravity current flows: the formation of large-scale three-dimensional structures. *Phys. Fluids* **33** (10), 106601.

MEIBURG, E., RADHAKRISHNAN, S. & NASR-AZADANI, M. 2015 Modeling gravity and turbidity currents: computational approaches and challenges. *Appl. Mech. Rev.* **67** (4), 040802.

https://doi.org/10.1017/jfm.2025.10393 Published online by Cambridge University Press

MORE, R.V. & ARDEKANI, A.M. 2023 Motion in stratified fluids. *Annu. Rev. Fluid Mech.* **55** (1), 157–192.
NASR-AZADANI, M.M. & MEIBURG, E. 2014 Turbidity currents interacting with three-dimensional seafloor topography. *J. Fluid Mech.* **745**, 409–443.
NASR-AZADANI, M.M., MEIBURG, E. & KNELLER, B. 2018 Mixing dynamics of turbidity currents interacting with complex seafloor topography. *Environ. Fluid Mech.* **18** (1), 201–223.
NECKER, F., HÄRTEL, C., KLEISER, L. & MEIBURG, E. 2002 High-resolution simulations of particle-driven gravity currents. *Intl J. Multiphase Flow* **28** (2), 279–300.
NECKER, F., HÄRTEL, C., KLEISER, L. & MEIBURG, E. 2005 Mixing and dissipation in particle-driven gravity currents. *J. Fluid Mech.* **545**, 339–372.
OOI, S.K., CONSTANTINESCU, G. & WEBER, L. 2009 Numerical simulations of lock-exchange compositional gravity current. *J. Fluid Mech.* **635**, 361–388.
OTTOLENGHI, L., ADDUCE, C., INGHILESI, R., ROMAN, F. & ARMENIO, V. 2016 Mixing in lock-release gravity currents propagating up a slope. *Phys. Fluids* **28** (5), 056604.
PARKER, D.A., BURRIDGE, H.C., PARTRIDGE, J.L. & LINDEN, P.F. 2020 A comparison of entrainment in turbulent line plumes adjacent to and distant from a vertical wall. *J. Fluid Mech.* **882**, A4.
PARKER, G., FUKUSHIMA, Y. & PANTIN, H.M. 1986 Self-accelerating turbidity currents. *J. Fluid Mech.* **171**, 145–181.
PELMARD, JOË, NORRIS, S. & FRIEDRICH, H. 2020 Statistical characterisation of turbulence for an unsteady gravity current. *J. Fluid Mech.* **901**, A7.
RICHARDSON, J. & HUNT, G.R. 2022 What is the entrainment coefficient of a pure turbulent line plume? *J. Fluid Mech.* **934**, A11.
SALIZZONI, P., VAUX, S., CREYSSELS, M., CRASKE, J. & VAN REEUWIJK, M. 2024 Entrainment in variable-density jets. *J. Fluid Mech.* **995**, A11.
SHIN, J.O., DALZIEL, S.B. & LINDEN, P.F. 2004 Gravity currents produced by lock exchange. *J. Fluid Mech.* **521**, 1–34.
SHRINGARPURE, M., CANTERO, M.I. & BALACHANDAR, S. 2012 Dynamics of complete turbulence suppression in turbidity currents driven by monodisperse suspensions of sediment. *J. Fluid Mech.* **712**, 384–417.
SHRINGARPURE, M., CANTERO, M.I. & BALACHANDAR, S. 2015 Analysis of turbulence suppression in sediment-laden saline currents. *Procedia Engng.* **126**, 16–23.
SHRINGARPURE, M., CANTERO, M.I. & BALACHANDAR, S. 2019 Equivalence of turbulence statistics between monodisperse and polydisperse turbidity currents. *Adv. Water Resour.* **129**, 385–399.
TSAI, Y.-H. & CHOU, Y.-J. 2025 On the suspension and deposition within turbidity currents. *J. Fluid Mech.* **1003**, A1.
WELLS, M.G. & DORRELL, R.M. 2021 Turbulence processes within turbidity currents. *Annu. Rev. Fluid Mech.* **53** (1), 59–83.
XIE, J., HU, P. & PAN, D. 2025 Coupling regimes between particles and Kelvin–Helmholtz billows in turbidity currents at moderate Reynolds number. (under review).
XIE, J., HU, P., ZHU, C., YU, Z. & PÄHTZ, T. 2023*a* Turbidity currents propagating down an inclined slope: particle auto-suspension. *J. Fluid Mech.* **954**, A44.
XIE, J., ZHU, C., HU, P., YU, Z. & PAN, D. 2023*b* Particle segregation within bidisperse turbidity current evolution. *J. Fluid Mech.* **971**, A16.
ZHOU, Z.Y., KUANG, S.B., CHU, K.W. & YU, A.B. 2010 Discrete particle simulation of particle–fluid flow: model formulations and their applicability. *J. Fluid Mech.* **661**, 482–510.

https://doi.org/10.1017/jfm.2025.10393 Published online by Cambridge University Press